minerals

MDPI

Article

Mineralogy of Zirconium in Iron-Oxides: A Micron- to Nanoscale Study of Hematite Ore from Peculiar Knob, South Australia

William Keyser [1,*], Cristiana L. Ciobanu [1], Nigel J. Cook [1], Holly Feltus [2], Geoff Johnson [2], Ashley Slattery [3], Benjamin P. Wade [3] and Kathy Ehrig [4]

1 School of Chemical Engineering, The University of Adelaide, Adelaide, SA 5005, Australia; cristiana.ciobanu@adelaide.edu.au (C.L.C.); nigel.cook@adelaide.edu.au (N.J.C.)
2 Formerly Arrium Mining, now SIMEC Mining, Level 2, 169 Fullarton Road, Dulwich, SA 5065, Australia; holly.feltus@simecmining.com (H.F.); geoff.johnson@simecmining.com (G.J.)
3 Adelaide Microscopy, The University of Adelaide, Adelaide, SA 5005, Australia; ashley.slattery@adelaide.edu.au (A.S.); benjamin.wade@adelaide.edu.au (B.P.W.)
4 BHP Olympic Dam, Adelaide, SA 5000, Australia; Kathy.J.Ehrig@bhpbilliton.com
* Correspondence: william.keyser@adelaide.edu.au; Tel.: +61-8-8313-3093

Received: 1 April 2019; Accepted: 17 April 2019; Published: 19 April 2019

Abstract: Zirconium is an element of considerable petrogenetic significance but is rarely found in hematite at concentrations higher than a few parts-per-million (ppm). Coarse-grained hematite ore from the metamorphosed Peculiar Knob iron deposit, South Australia, contains anomalous concentrations of Zr and has been investigated using microanalytical techniques that can bridge the micron- to nanoscales to understand the distribution of Zr in the ore. Hematite displays textures attributable to annealing under conditions of high-grade metamorphism, deformation twins (r~85° to hematite elongation), relict magnetite and fields of sub-micron-wide inclusions of baddeleyite as conjugate needles with orientation at ~110°/70°. Skeletal and granoblastic zircon, containing only a few ppm U, are both present interstitial to hematite. Using laser-ablation inductively coupled plasma mass spectrometry (LA-ICP-MS) spot analysis and mapping, the concentration of Zr in hematite is determined to be ~260 ppm on average (up to 680 ppm). The Zr content is, however, directly attributable to nm-scale inclusions of baddeleyite pervasively distributed throughout the hematite rather than Zr in solid solution. Distinction between nm-scale inclusions and lattice-bound trace element substitutions cannot be made from LA-ICP-MS data alone and requires nanoscale characterization. Scandium-rich (up to 0.18 wt. % Sc_2O_3) cores in zircon are documented by microprobe analysis and mapping. Using high-angle annular dark field scanning transmission electron microscopy imaging (HAADF-STEM) and energy-dispersive spectrometry STEM mapping of foils prepared in-situ by focused ion beam methods, we identify $[0\bar{1}1]_{baddeleyite}$ epitaxially intergrown with $[2\bar{2}.1]_{hematite}$. Lattice vectors at 84–86° underpinning the epitaxial intergrowth orientation correspond to directions of r-twins but not to the orientation of the needles, which display a ~15° misfit. This is attributable to directions of trellis exsolutions in a precursor titanomagnetite. U–Pb dating of zircon gives a $^{206}Pb/^{238}U$ weighted mean age of 1741 ± 49 Ma (sensitive high-resolution ion microprobe U–Pb method). Based on the findings presented here, detrital titanomagnetite from erosion of mafic rocks is considered the most likely source for Zr, Ti, Cr and Sc. Whether such detrital horizons accumulated in a basin with chemical precipitation of Fe-minerals (banded iron formation) is debatable, but such Fe-rich sediments clearly included detrital horizons. Martitization during the diagenesis-supergene enrichment cycle was followed by high-grade metamorphism during the ~1.73–1.69 Ga Kimban Orogeny during which martite recrystallized as granoblastic hematite. Later interaction with hydrothermal fluids associated with ~1.6 Ga Hiltaba-granitoids led to W, Sn and Sb enrichment in the hematite. By reconstructing the evolution of the massive orebody at Peculiar

Knob, we show how application of complimentary advanced microanalytical techniques, in-situ and on the same material but at different scales, provides critical constraints on ore-forming processes.

Keywords: hematite; Zr; baddeleyite; zircon; trace elements; HAADF-STEM; Peculiar Knob

1. Introduction

Despite zirconium (Zr) being an element of major petrogenetic interest, there is remarkably little published data on the concentration of Zr in the common iron-oxides, magnetite (Fe_3O_4) and hematite (α-Fe_2O_3). Dawson et al. [1] report a maximum of 0.21 wt. % ZrO_2 in magnetite from African carbonatites, and Reguir et al. [2] present LA-ICP-MS data for magnetite in calciocarbonatite from the Kerimasi volcano, Tanzania, showing that magnetite is a minor host for Zr (490 ppm). Data for Zr incorporation in hematite is particularly scarce. Selmi et al. [3] note up to 25 ppm Zr in hematitite from Quadrilátero Ferrífero iron formations in Brazil, while Cabral and Rosière [4] show values of <10 ppm in specular hematite from Tilkerode, Germany. Comparably low concentrations of Zr are found in iron-oxides from deposits from South Australia. These include, <10 ppm Zr within U-W-Sn-Mo-oscillatory-zoned hematite from the iron-oxide copper gold (IOCG) deposit at Olympic Dam [5] and <10 ppm (but up to ~18 ppm within individual samples) in hematite from banded iron formation (BIF)-derived ores in the Middleback Ranges, Eyre Peninsula [6]. In Fe–Ti deposits hosted by layered intrusions, e.g., Panzhihua, China [7], ilmenite exsolved from titanomagnetite will preferentially concentrate Zr (80–260 ppm) relative to host titanomagnetite (a few ppm at most). Phase diagrams of the systems ZrO_2–FeO and FeO–Fe_2O_3–ZrO_2–SiO_2 show solubility of Zr in iron-oxides at high temperatures [8,9] but have limited relevance to establishing solubility limits under crustal conditions (e.g., 10.3 mol. % ZrO_2 in FeO at 1332 °C).

The Peculiar Knob iron deposit [10] is located ~85 km SE of Coober Pedy within the Mount Woods Inlier of the Gawler Craton, South Australia (Figure 1). The deposit hosts an indicated and inferred resource of 20.9 Mt at an average of 62.95% Fe [11]. The deposit is a metamorphosed iron formation recognized by a prominent aeromagnetic anomaly. The high-grade hematite shows magnetic properties that have been interpreted, based on thermoremanent magnetization (TMR) properties and high Koenigsberger ratios [12], to indicate cooling from temperatures in excess of 680 °C. Peculiar Knob is also of interest as it occurs in a Paleoproterozoic terrane with a complex and much-debated geological history.

In the present contribution, anomalous concentrations of Zr and other trace elements have been measured in a sample containing coarse hematite representing massive iron ores similar to those investigated by Schmidt et al. [12]. We have undertaken a detailed multi-technique microanalytical study at the micron- to nanoscale following an approach analogous to that in Ciobanu et al. [13]. We address the petrography and geochemistry of hematite and the mineralogy of Zr in the ore with the objective of constraining deposit genesis. Understanding the incorporation of Zr in, and release from, iron-oxides in a complex ancient terrane represents a potential tool with broad petrogenetic application.

2. Geological Background

The several iron orebodies comprising the Peculiar Knob deposit are hosted within a poly-metamorphosed and -deformed supracrustal basement complex of Paleoproterozoic age. Basement consists of the Skylark Metasediments, various intrusive rock types, and the overlying Coodnambanna Metaconglomerate. Sequences comprising the Skylark Metasediments include quartz-magnetite-feldspar-clinopyroxene-orthopyroxene-apatite units, assigned to BIF [14,15]. The precise stratigraphy of the complex is, however, poorly constrained due to sparse outcrop at surface. Although the Skylark Metasediments are often correlated with Archean, marine-derived sediments (BIFs) of the Middleback Ranges, ~300 km south in the eastern Eyre Peninsula [16–18],

the current maximum deposition ages for these rocks (~1750 Ma [19]) suggests they are more likely equivalents to the Wallaroo Group metasediments of the Yorke Peninsula. Intrusive rocks recognized within the basement complex include the foliated 1691 ± 25 Ma Engenina Adamellite and the weakly- to non-foliated 1584 ± 18 Ma Balta Granite, affiliated with the ~1.6 Ga Hiltaba Suite [20].

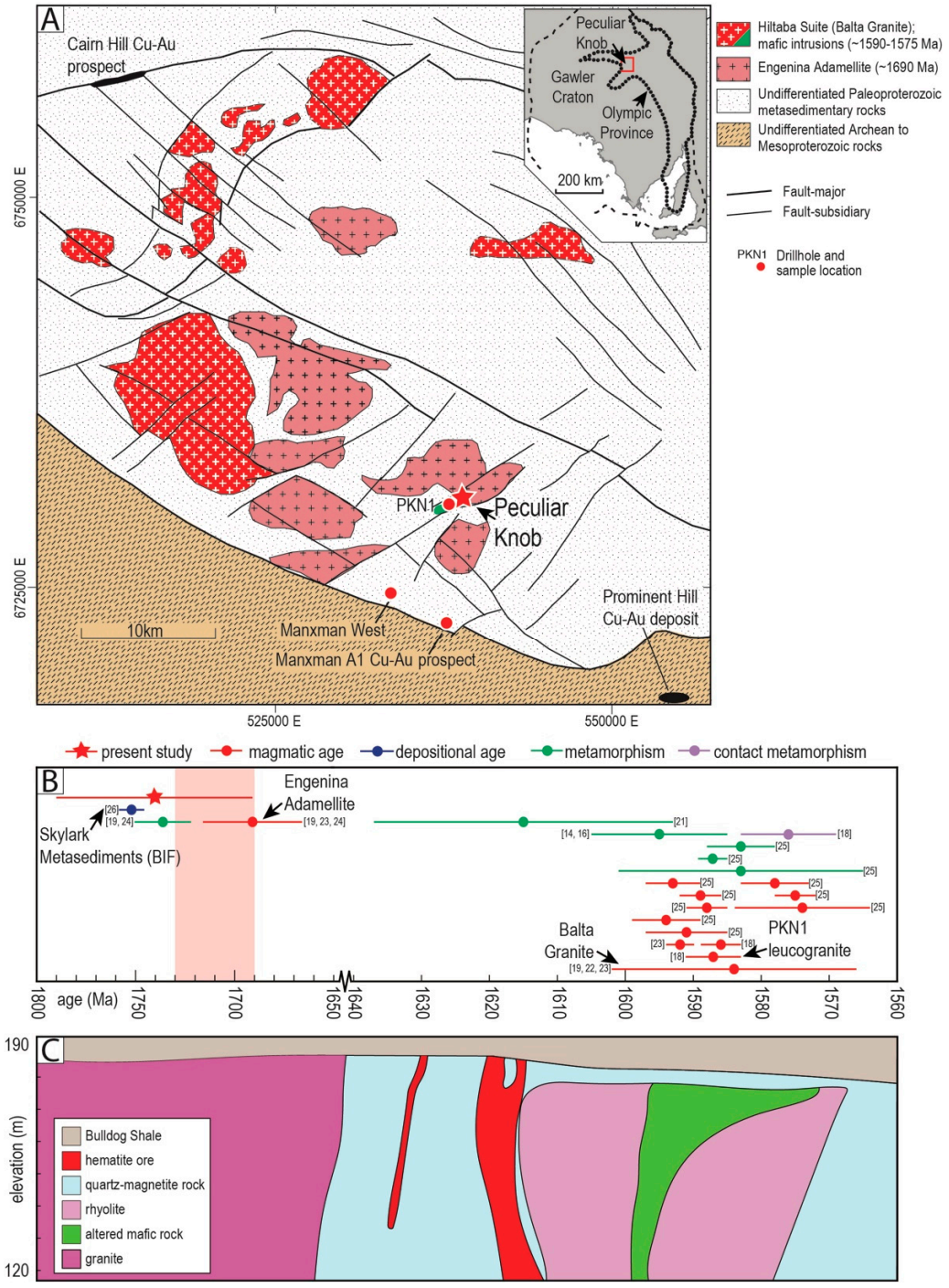

Figure 1. (**A**) Simplified geological map of the Mount Woods Inlier showing location of Peculiar Knob (PK) and other Cu–Au deposits/prospects (modified after [21]). (**B**) Summary of published metamorphic and igneous ages for the Mount Woods Inlier, modified after [22] and data sourced from Ambrose and Flint [23], Fanning et al. [24], Fanning [20], Finlay [25], Holm [26], Jagodzinski [19], Jagodzinski et al. [27], Chalmers [15] and Forbes et al. [22]. (**C**) Schematic cross-section through one of the PK orebodies showing host lithologies (data from Nielson [11]).

The metamorphic history of the Mount Woods Inlier has been extensively debated but is nevertheless important in the context of understanding and constraining sequences of mineralization at Peculiar Knob (Figure 1B). The metamorphic grade within the Mount Woods Inlier is suggested to increase from greenschist facies in the south to granulite facies in the north [28]. Granulite facies metamorphism occurred coincident with early stages of the ~1.73–1.69 Ga Kimban Orogeny ([29] and references therein), based on a 1736 ± 14 Ma SHRIMP (sensitive high-resolution ion microprobe) U–Pb age of interpreted metamorphic zircon [20].

Metamorphic ages of ~1.59 Ga are reported from throughout the Mount Woods Inlier [19,26,27]. Recent monazite CHIME (chemical Th–U-total Pb isochron method) dating, combined with P-T pseudosection modeling of a sample of Skylark Metasediments, provided evidence for a granulite facies metamorphic event that peaked at ~1595 Ma [22]. This sample, however, derived from a location some distance northwest from Peculiar Knob. A potentially still younger overprint is indicated by metamorphic rims dated at 1576.2 ± 7 Ma from a leucogabbro from drillhole PKN1 adjacent to the deposit [27].

The deposit is buried beneath 12–35 m of the flat-lying Cretaceous sediments (Bulldog Shale) and was mined between 2011 and 2015. The deposit consists of a zone of high-grade hematite mineralization, roughly 1 km in length, ~35 m wide and up to ~300 m deep (Figure 1C). The orebodies are steeply NW-dipping and occur as two NE-striking, sub-parallel elongated lensoidal bodies, which are off-set by at least four cross-cutting faults. These are hosted within a sequence of iron-rich units and various high-grade metamorphosed rocks and granitoids. Ultramafic/mafic lithologies within the sequence can be inferred by the presence of altered, chlorite-rich rocks. Similar lithologies are also known associated with BIF sequences from the Middleback Ranges deposits [6]. The ores comprise massive specular hematite and have been considered to represent the metamorphosed hydrothermally-altered equivalents of Fe-rich sediments, including chemical precipitates (BIFs), in several previous studies [10,15,30], and also in the most recent resource report [11]. Early studies also acknowledge the impact on the ores from the adjacent Balta Granite (e.g., [31]). More recently, other authors have speculated on the possible relationships between iron deposits such as Peculiar Knob and IOCG systems of the eastern Gawler Craton (e.g., [32]), although little direct evidence is available to support such a hypothesis.

3. Methodology

The present study was carried out on a sample of massive hematite ore (Figure 2) collected from the Peculiar Knob open pit. The sample was assayed by Intertek Genalysis (Adelaide, Australia). Methodology for the whole-rock analysis and element minimum detection limits (MDL) are provided in Supplementary Material A. All the below mentioned microanalytical instrumentation are housed at Adelaide Microscopy, The University of Adelaide (Adelaide, Australia). Petrographic observations were made on a one-inch polished block using reflected-light optical and scanning electron microscopy (SEM). A FEI Quanta 450 SEM equipped with an energy dispersive X-ray spectrometer (EDS) was used for further μm-scale observations, detection of compositional zonation within hematite and zircon, and for back-scattered electron (BSE) imaging. Analytical conditions for SEM work were 20 kV acceleration voltage and a beam current of 10 nA.

Trace element concentrations in hematite were measured with a RESOlution excimer laser ablation system (Applied Spectra Inc., Fremont, SA, USA) coupled to an Agilent 7900x Quadrupole ICP-MS using a frequency of 10 Hz, fluence of 3.5 J/cm^2 and a spot diameter of 60 μm. Laser ablation element maps were performed using a laser frequency of 10 Hz, fluence of ~3 J/cm^2, and a spot diameter and scan speed of 7 μm and 7 μm/s, respectively. ^{57}Fe was used as an internal standard element for quantification of hematite assuming ideal stoichiometry. External reference materials used were the synthetic basalt glass standard GSD-1G glass (USGS; [33]) and the NIST-610 glass [34]. "GLITTER" software [35] was used for data reduction. To avoid element contamination from trace minerals included in hematite, only those intervals within individual spot analyses showing flat signals were selected during the data reduction process. Time-resolved depth profiles were used to further

assess trace element data quality and to ensure negligible influence from included minerals during analysis. Average minimum detection limits (MDL) for the analyzed elements are also provided in the same appendix. Laser ablation element maps were constructed using "Iolite" software [36]. See Supplementary Material A for full details of analytical methods.

Zircon compositions were quantitatively determined using a Cameca SX-Five Electron Microprobe (Adelaide Microscopy) running "PeakSite" software and equipped with five wavelength-dispersive X-Ray detectors. Calibration and data reduction were carried out using "Probe for EPMA" software. Analytical conditions, elements measured, average MDL, peak/background positions, count times, and standards are listed in Supplementary Material A.

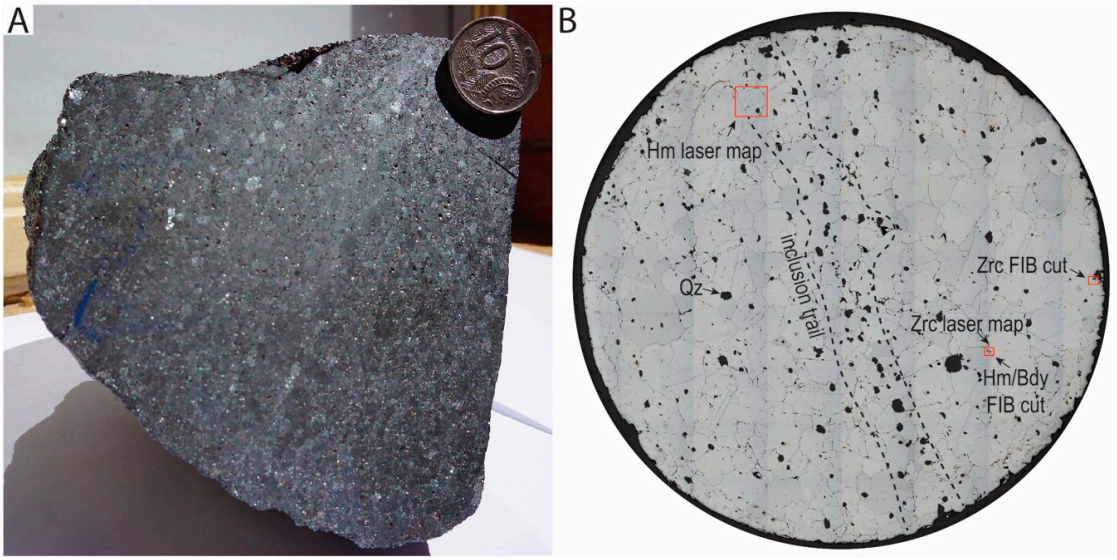

Figure 2. (**A**) Hand-specimen photograph of the studied hematite ore (cut face). (**B**) Reflected light photograph of one-inch polished block showing coarseness of granoblastic hematite. Note gangue as (i) interstitial grains (mostly quartz (Qz), black), and (ii) an array of dense grains throughout hematite (arrowed). Areas with analyzed zircon and the focused ion beam cuts in hematite (Hm)/baddeleyite (Bdy) and zircon (Zrc) are also marked.

A FEI-Helios nanoLab Dual Focused Ion Beam (FIB) SEM was used for preparing foils for transmission electron microscopy (TEM) study. Procedures for extracting and thinning (to <100 nm) of foils by beam (Ga^+) milling and attachment to Cu grids followed those outlined previously [37]. High-angle annular dark field-scanning transmission electron microscopy (HAADF-STEM) imaging and energy-dispersive X-ray spectrometry (EDS)-STEM mapping were performed on a high-resolution, probe-corrected, FEI Titan Themis S/TEM equipped with the X-FEG Schottky source and Super-X EDS geometry, operated at 200 kV.

Cathodoluminescence (CL) imaging to characterize core-rim relationships and zonation patterns within granular zircon interstitial to hematite was performed on a FEI Quanta 600 MLA SEM (Adelaide Microscopy) equipped with a tungsten filament electron source. In-situ U–Pb dating of zircon was performed with the high-resolution ion microprobe (SHRIMP-II) at the John de Laeter Centre, Bentley, Curtin University, Western Australia. Analytical methods used broadly follow those described by Compston et al. [38] and Williams [39]. Further details are given in Supplementary Material A.

4. Results

4.1. Petrography

The massive ore consists of mm-sized, polyhedral grains of hematite with granoblastic texture (Figure 2). Gangue minerals (mostly quartz and minor siderite) are located at hematite grain boundaries

or concentrated along trails within the hematite (Figure 2B). Mutual grain boundaries, often with triple junctions at 120°, exhibit both straight and serrated margins (Figure 3A,B). Polysynthetic twinning, following one or two crystallographic directions, is a common feature of hematite (Figure 3A–C). Small grains, from <1 µm to a few µm in size, of magnetite are ubiquitous throughout the hematite (Figure 3D–I). The morphology of these grains varies from thin lamellae to (sub)-euhedral grains of hexagonal to octagonal shape in cross-section. Magnetite is closely associated with the twin planes in hematite, either at their margins, along, or slightly offset/across them (Figure 3E–G). Pressure gashes filled with gangue minerals (quartz and siderite) and tiny blebs of magnetite are observed along microfractures crosscutting the twin planes (Figure 3I).

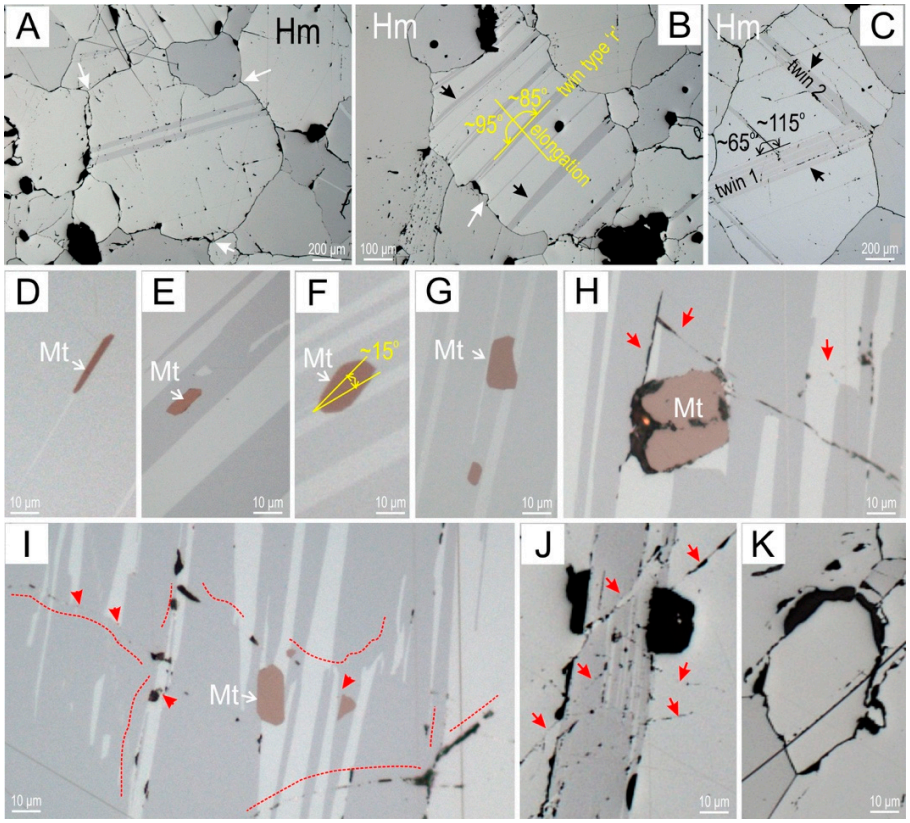

Figure 3. Reflected light microphotographs showing petrographic aspects of hematite (Hm). (**A**) Granoblastic texture with triple junctions at 120° (white arrows) and straight boundaries. (**B**) Serrated boundaries (white arrows) around a grain with dense twins (black arrows). Note orientation of twin plane relative to Hm elongation as marked, attributable to rhombohedral (r) twins. (**C**) Two sets of twins with angles as marked in coarse Hm with different orientation to the grain in (**B**). (**D**–**I**) Magnetite (Mt) grains associated with twin planes. Note varying morphologies from acicular, in (**D**), to (sub)euhedral, and changing relationships with the twin planes, i.e., along the twin planes in (**D**) and (**E**), slightly offset as marked in (**F**) and (**G**), and across them in (**H**). Rounding and marginal replacement of Mt in (**H**) is associated with microfractures (red arrows). (**I**) Microfractures (red lines) marked by pressure gashes filled with gangue minerals and tiny blebs of Mt (arrowed). Note that twins are displaced by the microfractures. (**J**) Microfractures oblique to twin boundaries (arrowed) producing intra-lamellar brecciation. Note the presence of gangue minerals (black) and pores along the fractures inferring fluid percolation. (**K**) Deformation of a small hematite grain associated with rounding and mantling by gangue.

Rounding and replacement of coarser magnetite by gangue is also observed at junctions of microfractures (Figure 3H). More advanced reworking of hematite is observed along the trail of gangue minerals that runs through the middle part of the polished block. This includes brecciation within

twin planes associated with small displacements of finer sets of twins (Figure 3J) and deformation of smaller hematite grains (Figure 3K).

One of the unusual characteristics of the hematite is the presence of fields comprised of micron to sub-micron inclusions with bright appearance on BSE images (Figure 4A–C). These are identified from the nanoscale study (see below) as baddeleyite (monoclinic ZrO_2). Such fields are, however, absent in some grains (Figure 4A), or are effectively invisible, at least at this scale of observation. The baddeleyite inclusions display bleb, or more often needle-like morphologies, are generally <3 μm in length and <1 μm in width and are preferentially oriented in two or three directions. The obtuse/acute angles between two arrays of inclusions are ~110°/70°.

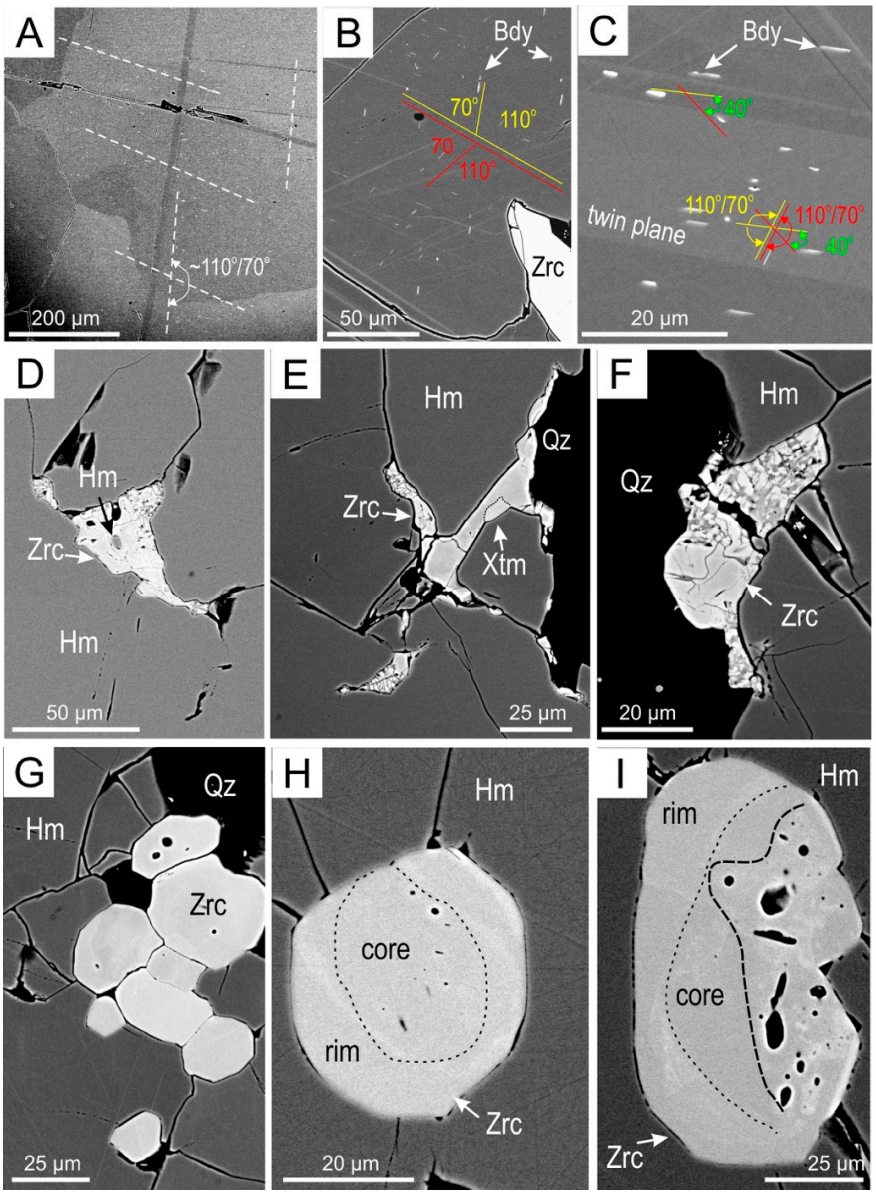

Figure 4. BSE images showing Zr-minerals in hematite (Hm) as baddeleyite (Bdy) inclusions (in **A**–**C**), and as zircon (Zrc) with skeletal and granular morphology (in **D**–**F** and **G**–**I**), respectively. Note the preferential arrangement of the Bdy needles (orientation angles as marked) across grain boundaries marked as dashed lines in (**A**), or along twin planes in Hm in (**C**). Note the lack of any direct contact between Bdy and Zrc when present in the same area in (**B**). Inclusions of Hm, xenotime-(Y) (Xtm) and fluorapatite (Ap) in zircon are associated with presence of pores and alteration. The boundary between core and rim in granular Zrc is marked by dashed lines in (**H**) and (**I**).

The baddeleyite arrays can cross over grain boundaries (Figure 4A), form locally denser domains within the same grain (Figure 4B), or be present within/along twin planes, remarkably with the same preferential orientation as elsewhere (Figure 4C). Some of the twins in hematite are also visible on BSE images (Figure 4C). Zircon is also present in the sample and displays morphology varying from skeletal (Figure 4D–F) to granular (Figure 4G–I). The skeletal zircon, restricted to grain boundaries in hematite or between hematite and quartz, features marginal alteration and tiny inclusions of hematite and xenotime-(Y) (Figure 4D,E). A transition from skeletal to granular morphology is observed towards the boundaries with quartz (Figure 4F). The granular zircon form aggregates towards larger quartz pockets (Figure 4G). Larger, single grains of zircon occur within hematite and these are surrounded by radial cracks (Figure 4H,I). Such grains display asymmetric cores and rims with brighter bands marking the two domains on BSE images. Fluorapatite, xenotime-(Y) and pores are noted particularly within the cores or towards corroded margins in zircon (Figure 4I).

Both hematite and quartz display textures indicative of fluid percolation (Figure 5A,B). Pores and inclusions of siderite and magnetite mark zones of microbrecciation within sets of twin lamellae (Figure 5A). Coarser quartz grains with partially resorbed/hooked boundaries display rotational textures comprising sub-µm size grains of hematite and acicular Ti-oxides (probably rutile) (Figure 5B–D). Hematite aggregates nucleate within pores in such quartz (Figure 5C). Siderite is present between hematite lamellae and also forms interstitial pockets with quartz (Figure 4E,F). Rotational textures between the two minerals are observed in the latter case (Figure 5F). Sub-rounded grains of fluorapatite are also noted within hematite (Figure 5G).

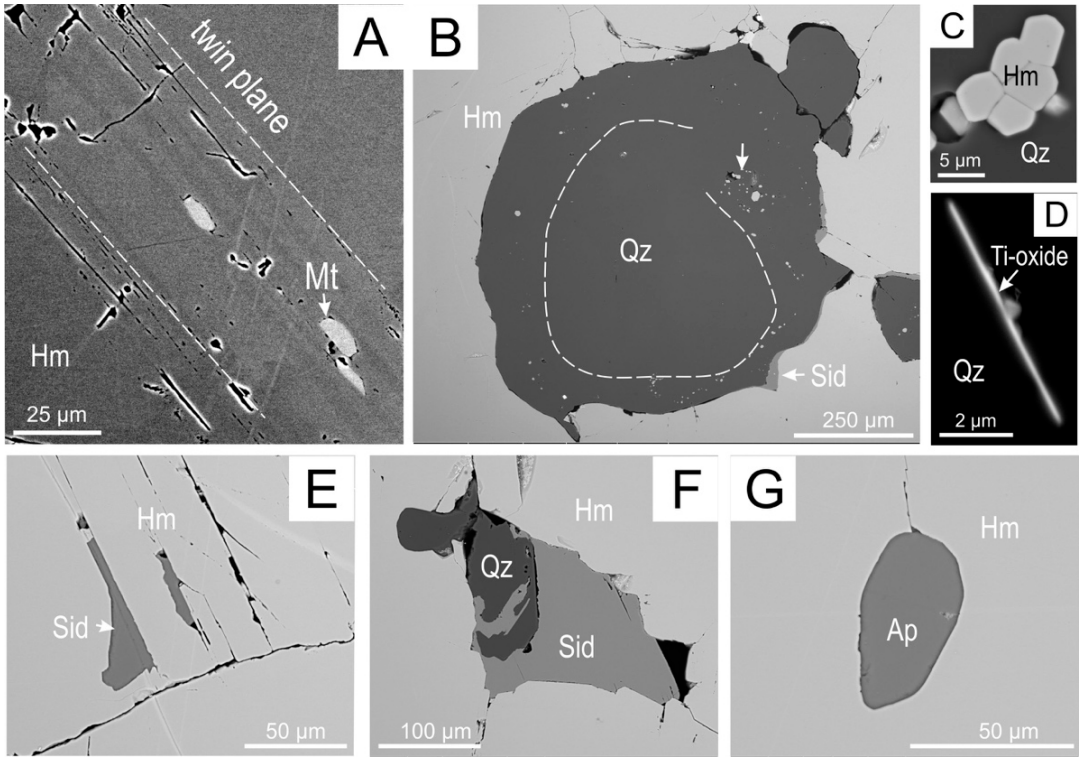

Figure 5. BSE images showing hematite overprint (**A**) and gangue minerals (**B**–**G**). (**A**) Brecciation of hematite (Hm) marked by pores and inclusions of magnetite (Mt). (**B**) Rotational texture in quartz (Qz) marked by trails of inclusions (dashed line). (**C**) Aggregate of hematite formed within a pore in Qz. (**E**) Typical needle of Ti-oxide in Qz. (**F**–**H**) Inclusions of siderite (Sid), Qz and fluorapatite (Ap) within Hm.

4.2. Geochemistry

4.2.1. Whole-Rock Data

Whole-rock geochemical data for the studied ore sample shows it is composed predominantly of Fe_2O_3 (Table 1). A minor amount of SiO_2 is present, which is represented mainly by quartz. Other components are TiO_2, P_2O_5 and CO_2, the latter two likely resulting from fluorapatite and carbonates, respectively. The oxides Al_2O_3, MgO, CaO, K_2O and MnO are present in concentrations <0.05 wt. %.

A suite of trace elements was measured at notable concentrations (Table 1). The chalcophile element Sb measured 7.5 ppm whereas typically associated As measured only 1 ppm. The transitional elements Cr and V are both present at concentrations ≥25 ppm. Besides relatively high TiO_2 (0.26 wt. %), other high-field strength elements (HFSE) that were measured, albeit at lower concentrations (<6 ppm), include Nb and Hf. Zirconium concentration in whole-rock is 94 ppm. Typical granite-related elements Sn (4 ppm) and W (4 ppm) are also present.

Table 1. Whole-rock major and trace element geochemistry.

Element (wt. %)		Element (ppm)									
SiO_2	0.96	Li	1.4	V	25	Sb	7.5	La	2.3	Tm	<0.05
Al_2O_3	0.06	Ba	1	Nb	5.8	Bi	<0.05	Ce	5.2	Yb	0.16
MgO	0.02	Sr	1.2	Ta	0.3	Pb	<5	Pr	0.55	Lu	0.03
Fe_2O_3	97.81	Be	<0.5	Zr	94	Te	0.1	Nd	2	ΣREE	12.8
CaO	0.01	Rb	<0.1	Hf	2.2	Se	<1	Sm	0.27		
K_2O	0.01	Cs	<0.05	Sc	<2	Tl	<0.02	Eu	0.08		
Na_2O	0.01	Cr	27	Ga	1.7	Mo	<1	Gd	0.21		
P_2O_5	0.16	Ni	<1	Ge	0.1	Re	<0.05	Tb	0.03		
TiO_2	0.26	Co	0.2	In	<0.05	Sn	4	Dy	0.22		
MnO	0.01	Cu	<1	Au	<0.01	W	4	Y	1.5		
LOI	0.03	Zn	<1	Ag	<0.1	Th	0.14	Ho	0.05		
Total + LOI	99.47	Cd	<0.05	As	1	U_3O_8	0.16	Er	0.18		

LOI: loss on ignition.

With the exception of La, Ce, Y and Nd, rare-earth elements occur at concentrations <1 ppm (ΣREE = 12.8 ppm). The chondrite-normalized REE fractionation trend shows LREE enrichment (La_{CN}/Yb_{CN} = 10.31) and no Ce- or Y-anomaly (Figure 6).

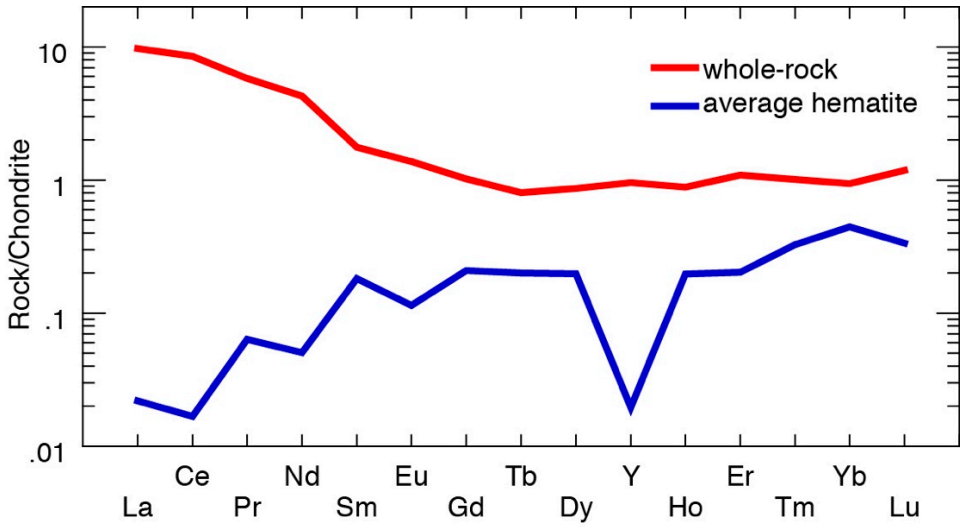

Figure 6. Chondrite-normalized REE fractionation trends for whole-rock and hematite. Chondrite values from [40]. Note the marked differences for LREE (high in whole-rock, low in hematite) and the negative Y-anomaly for hematite. These features are attributable to presence of Zr-minerals and fluorapatite.

4.2.2. Trace Element Concentrations and Grain-Scale Distribution in Hematite

LA-ICP-MS trace element compositional data for hematite show the presence of several elements that likely account for a large portion of the whole-rock budget (Table 2). Aluminum, Si, Cr, V and P measured in the tens to hundreds ppm. Antimony is present at a concentration more than an order of magnitude higher than As. Tin and W both measured ~5 ppm. Among the HFSE, Ti and Zr were measured at high concentrations, i.e., average ~1490 ppm and ~250 ppm, respectively; Nb and Hf measured at ~5 ppm. Zirconium concentration varies, as expected, depending upon the presence or absence of visible baddeleyite inclusions on the surface of the polished block, i.e., between 68 ppm up to 600 ppm. However, given the nm-size of baddeleyite inclusions, these are not observable as fluctuating signals for Zr on the time-resolved depth profiles for individual LA-ICP-MS spot analyses (Figure 7).

The concentrations of all other trace elements were <1 ppm. The chondrite-normalized REE fractionation trend for a mean analysis of hematite shows relative LREE depletion and HREE enrichment (La_{CN}/Yb_{CN} = 0.049), noticeable negative Ce-, Eu-anomalies and a strong negative Y-anomaly (Figure 6). The differences between the whole-rock and hematite data are attributable to the role of Zr-minerals (particularly Y) and fluorapatite (LREE).

Trace element LA-ICP-MS maps of hematite reveal grain-scale compositional zoning (Figure 8). This is expressed by relative enrichment in elements such as Zr, Hf, Ti and Cr in hematite cores and respective depletion of these elements on grain margins. The latter are, however, enriched in Nb, Sb, W and Sn. Although the fields with baddeleyite are visualized on the LA-ICP-MS element maps (Zr in Figure 8A), Zr is relatively homogenously distributed throughout hematite grain cores, as also shown by time-resolved depth profiles, with measurable, still high concentrations of Zr in hematite grains that are apparently free of baddeleyite (Figure 7). The maps also show that Zr and Hf are depleted along the margins of hematite wherever granular zircon is present (Figure 8B). Zircon grains on the maps illustrated in Figure 8B show rims that are enriched in U relative to cores.

Table 2. LA-ICP-MS trace element (ppm) data for hematite from Peculiar Knob.

Element	Geomean	Max.	Min.	s.t.d.	Element	Geomean	Max.	Min.	s.t.d.
Mg	6.3	48	1.3	11	Hf	6.7	24	1.3	6.6
Al	421	444	382	14	Ta	0.50	0.59	0.42	0.04
Si	206	325	174	32	W	5.0	9.4	1.1	2.4
P	14	22	9.6	3.1	^{206}Pb	0.24	1.3	0.05	0.30
Ca	63	99	40	30	^{208}Pb	0.17	0.66	0.04	0.16
Sc	1.1	1.5	1.0	0.15	Th	0.03	1.2	0.002	0.48
Ti	1492	1881	1218	124	U	0.06	1.0	0.002	0.29
V	36	39	34	1.2	La	0.005	0.03	0.002	0.007
Cr	22	40	16	4.7	Ce	0.01	0.13	0.002	0.04
Mn	3.1	3.9	2.4	0.41	Pr	0.006	0.02	0.001	0.007
Co	0.69	1.1	0.31	0.25	Nd	0.02	0.09	0.008	0.03
Ni	0.72	1.2	0.32	0.25	Sm	0.03	0.10	0.01	0.03
Cu	0.55	0.68	0.41	0.11	Eu	0.007	0.02	0.002	0.008
Zn	0.28	0.55	0.16	0.12	Gd	0.04	0.34	0.01	0.11
Ga	1.8	2.1	1.5	0.16	Tb	0.007	0.08	0.002	0.03
As	1.3	3.4	0.44	0.78	Dy	0.05	0.58	0.006	0.20
Sr	0.03	0.55	0.01	0.16	Y	0.03	5.6	0.003	1.5
Zr	260	609	68	145	Ho	0.01	0.09	0.002	0.03
Nb	5.3	5.9	4.2	0.40	Er	0.03	0.56	0.005	0.19
Mo	0.76	1.0	0.59	0.09	Tm	0.008	0.09	0.002	0.03
Sn	6.4	11	4.8	1.6	Yb	0.08	0.77	0.01	0.25
Sb	20	25	12	3.2	Lu	0.009	0.14	0.002	0.04
Ba	0.16	0.53	0.08	0.16					
(n = 20 hematite analyses)									

Geomean: geometric mean; s.t.d.: standard deviation; Max.: maximum; Min.: minimum.

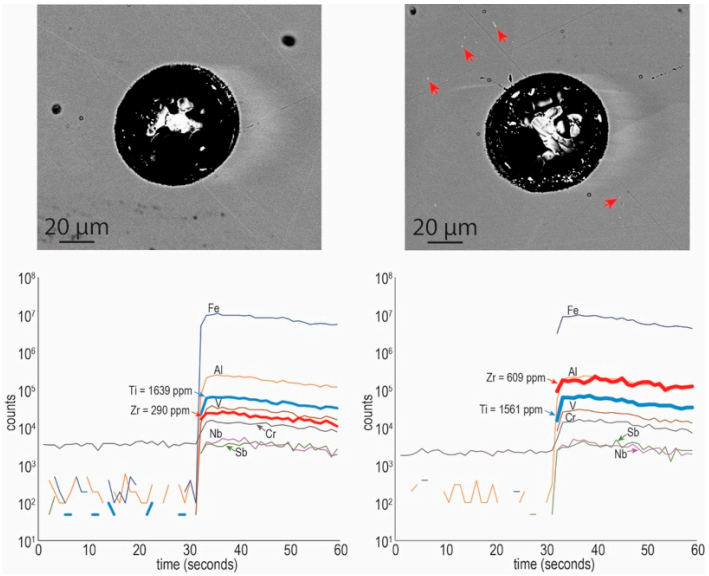

Figure 7. BSE images and representative time-resolved depth profiles of (**left**) "clean" hematite and (**right**) hematite with baddeleyite inclusions (marked by red arrows). Note the smooth signal for Zr in both cases but a difference in the intensity of the signal, which is an order of magnitude higher in the second case. Titanium shows comparable smooth signals and similar count intensity in both cases.

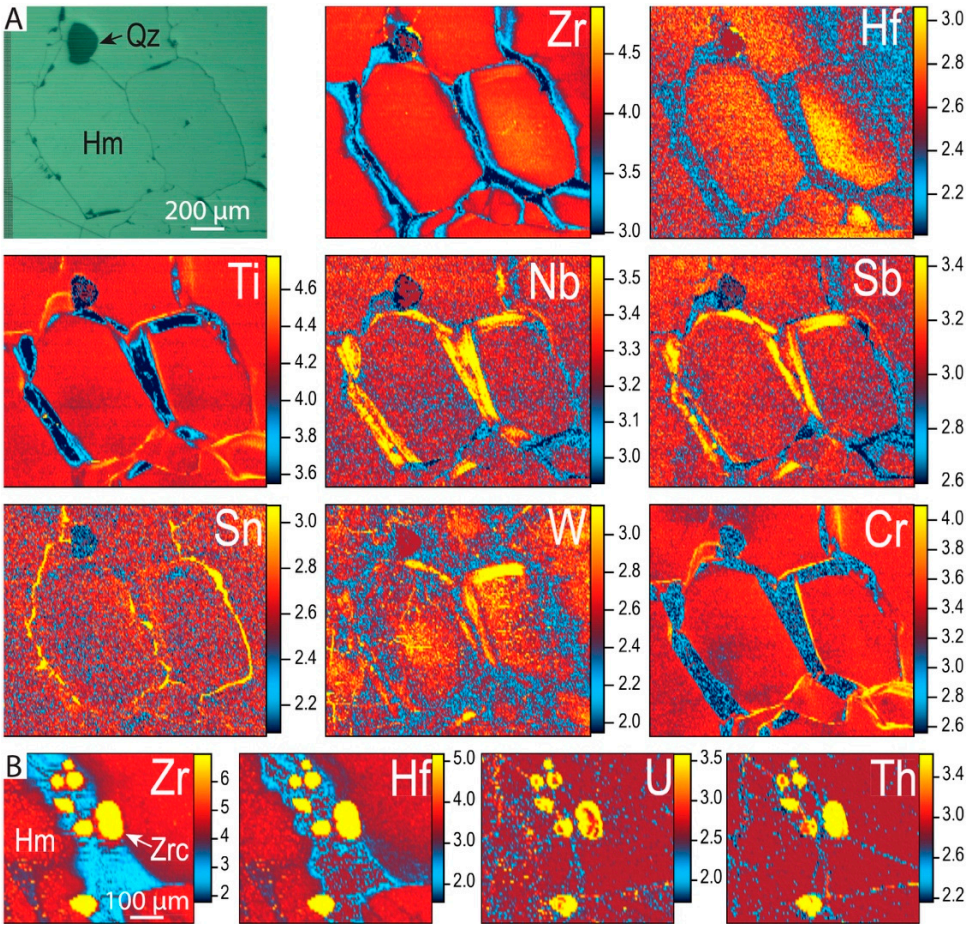

Figure 8. (**A**) Reflected light image (top left) and LA-ICP-MS element maps of granoblastic hematite (Hm) showing hematite cores enriched in Zr, Hf, Ti and Cr, with margins depleted in these elements but enriched in Nb, Sb, Sn and W. (**B**) LA-ICP-MS element maps showing aggregates of granular zircon (Zrc) along hematite margins that are depleted in Zr and Hf. Scales in counts-per second.

4.2.3. Zircon Electron Microprobe Data

Electron microprobe spot analysis (Table 3) and mapping of the various zircon textures show distinct compositional differences between the cores and rims of granular and skeletal zircon (Figures 9 and 10). Besides ZrO_2 and SiO_2, all textural variants of zircon contain measurable concentrations of MgO (~0.02 wt. %) and HfO_2 (~1.5 wt. %). The cores of granular zircon, however, contain higher concentrations of Al_2O_3 (~0.2 wt. %), P_2O_5 (~0.5 wt. %) and Y_2O_3 (0.05 wt. %) relative to the rims of the same grains and also the skeletal zircon. Additionally, Sc_2O_3 (~0.1 wt. %) was measured in zircon cores whereas rims and skeletal zircon measured below detection limit.

The core and rim textures in granular zircon are well-marked on the maps, particularly by the presence of Sc (Figure 9). The boundary between the core and rim is marked by depletion in P, but enrichment in U corresponding to the bright and dark zones on BSE and CL images, respectively (Figure 9). The highest concentrations of P, Al and Y occur along the grain boundaries and cracks suggesting secondary element remobilization from zircon. Occurrence of xenotime-(Y) along the margin of zircon is common (e.g., the BSE image in Figure 10). The area mapped for the skeletal zircon (Figure 10) can be considered as transitional toward the granular texture. This shows comparable trace element enrichment as in the granular type but with a patchy appearance, also due to the much smaller size of the map. Notable is the marginal enrichment in P, Al and Y on one side of the zircon.

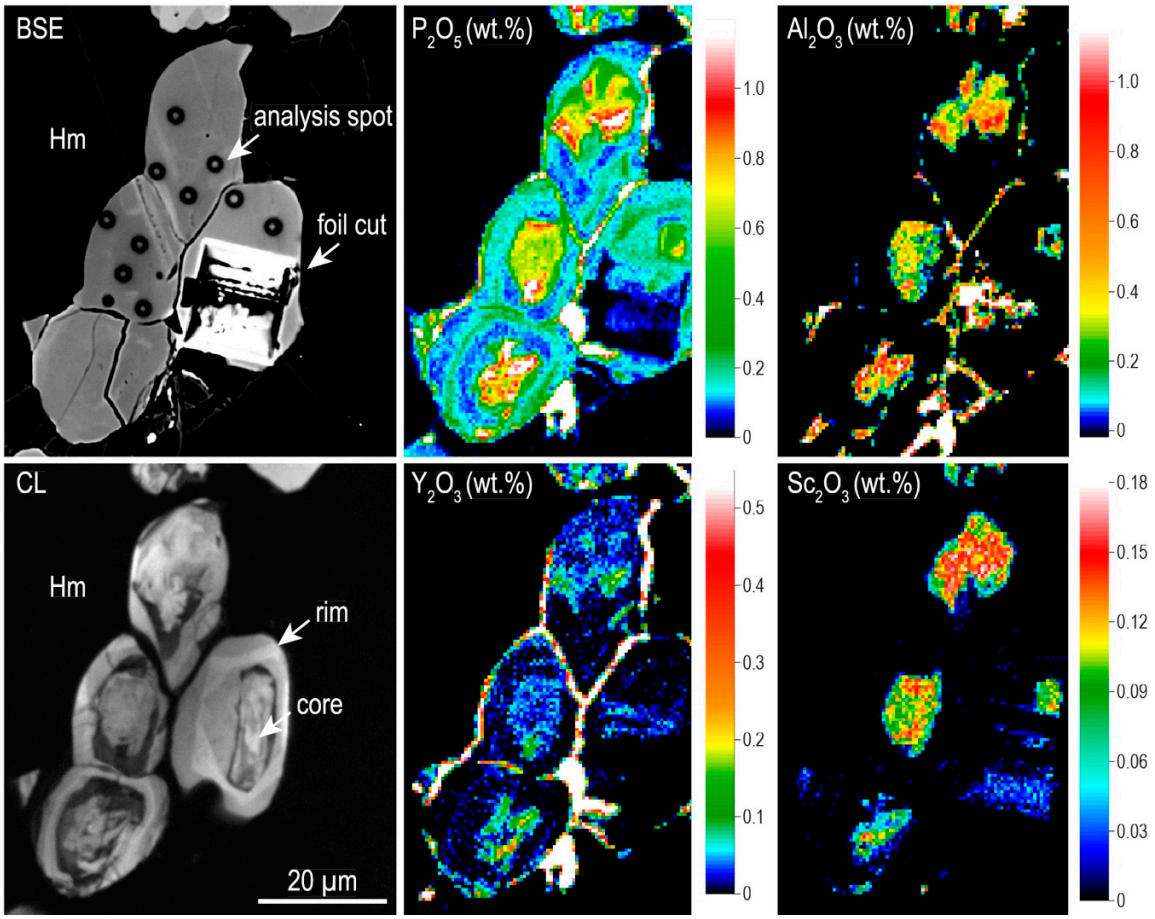

Figure 9. EPMA element map of granular zircon from the studied hematite (Hm) ore. Top left image is a BSE image showing analysis spots and location of foil cut via FIB and described in Section 4.3. The CL image of the same aggregate is shown in the bottom left panel. Note the core and rim textures with a dark ring on CL image and slightly brighter appearance on BSE image corresponding to U-richer zones in zircon. The maps reveal the clear geochemical differences between cores and rims in the granular zircon. Scales in wt. %.

Table 3. Electron microprobe data for zircon.

Texture	**Granular**										**Skeletal**		
	Core					**Rim**							
#	**1**	**2**	**3**	**4**	**5 ****	**1**	**2**	**3**	**4**	**5**	**1**	**2**	**3**
SiO_2	32.91	33.76	33.16	33.15	29.47	33.64	33.18	33.32	33.08	33.73	33.52	33.09	33.37
Al_2O_3	0.25	0.27	0.28	0.26	0.09	0.19	0.19	0.18	0.24	0.21	<mdl	<mdl	0.19
Fe_2O_3 *	1.33	1.25	0.81	0.88	2.18	0.67	1.96	1.26	1.11	1.06	1.55	1.03	0.80
MgO	0.05	0.03	0.05	0.05	0.02	0.02	0.02	0.01	0.02	0.03	0.01	0.01	0.02
CaO	<mdl	<mdl	0.01	<mdl	0.09	0.02	<mdl	<mdl	0.01	<mdl	<mdl	0.03	<mdl
Na_2O	<mdl	0.03	<mdl	0.02	0.05	<mdl	<mdl	<mdl	0.02	<mdl	0.04	0.05	<mdl
P_2O_5	0.72	0.51	0.69	0.70	0.23	0.08	0.18	0.10	0.18	0.13	0.17	0.09	0.10
Sc_2O_3	0.18	0.13	0.11	0.13	0.03	<mdl	<mdl	<mdl	<mdl	<mdl	<mdl	<mdl	<mdl
ZrO_2	65.85	65.35	65.92	65.86	65.73	65.94	65.67	66.42	65.35	66.53	67.35	67.03	66.39
HfO_2	1.36	1.40	1.46	1.55	0.98	1.39	1.64	1.65	1.73	1.77	0.99	1.03	1.55
PbO	<mdl	0.02	<mdl	0.03	<mdl	0.02	0.02	<mdl	0.02	<mdl	<mdl	<mdl	<mdl
Y_2O_3	0.04	0.03	0.05	0.06	0.10	0.02	0.02	0.01	0.16	0.01	0.06	0.03	0.02
Eu_2O_3	<mdl	<mdl	<mdl	<mdl	<mdl	<mdl	<mdl	<mdl	<mdl	<mdl	<mdl	0.04	<mdl
Gd_2O_3	<mdl	<mdl	<mdl	<mdl	0.05	0.05	<mdl	<mdl	<mdl	<mdl	0.07	<mdl	<mdl
Tb_2O_3	0.03	<mdl	<mdl	<mdl	0.07	<mdl	0.04	<mdl	<mdl	<mdl	<mdl	<mdl	0.03
Dy_2O_3	0.05	<mdl	<mdl	<mdl	<mdl	0.03	0.04	<mdl	<mdl	0.03	<mdl	<mdl	<mdl
Er_2O_3	0.05	<mdl	0.03	0.03	<mdl	<mdl	0.05	<mdl	0.05	0.03	0.03	<mdl	<mdl
Yb_2O_3	0.09	0.09	0.09	0.11	<mdl	0.06	0.06	<mdl	0.09	0.04	<mdl	<mdl	0.05
Cl	<mdl	<mdl	<mdl	<mdl	<mdl	0.01	<mdl	<mdl	<mdl	<mdl	<mdl	0.01	<mdl
Total	101.58	101.62	101.84	101.96	96.91	101.47	101.11	101.69	100.95	102.51	102.23	101.42	101.73
Zircon formula: (ABZ_4); calculated based on 4 oxygen per formula unit													
Al	0.009	0.010	0.010	0.009	0.003	0.007	0.007	0.006	0.008	0.007	-	-	0.007
Mg	0.002	0.001	0.002	0.002	0.001	0.001	0.001	-	0.001	0.001	0.001	-	0.001
Ca	-	-	-	-	0.003	0.001	-	-	-	-	-	0.001	-
Na	-	0.001	-	0.001	0.003	-	-	-	0.001	-	0.002	0.003	-
Sc	0.005	0.003	0.003	0.003	0.001	-	-	-	-	-	-	-	-
Zr	0.964	0.952	0.962	0.960	1.029	0.967	0.969	0.975	0.966	0.968	0.982	0.987	0.974
Hf	0.012	0.012	0.012	0.013	0.009	0.012	0.014	0.014	0.015	0.015	0.008	0.009	0.013
Pb	-	-	-	-	-	-	-	-	-	-	-	-	-
Y	0.001	0.001	0.001	0.001	0.002	-	-	-	0.003	-	0.001	0.001	-
Eu	-	-	-	-	-	-	-	-	-	-	-	-	-
Gd	-	-	-	-	0.001	-	-	-	-	-	0.001	-	-
Tb	-	-	-	-	-	-	-	-	-	-	-	-	-
Dy	-	-	-	-	-	-	-	-	-	-	-	-	-
Er	0.001	-	-	-	-	-	0.001	-	-	-	-	-	-
Yb	0.001	0.001	0.001	0.001	-	0.001	0.001	-	0.001	-	-	-	-
Tot. (A site)	0.994	0.981	0.991	0.992	1.052	0.989	0.993	0.996	0.996	0.993	0.995	1.001	0.996
ΣREY	0.003	0.001	0.002	0.002	0.002	0.002	0.002	0.000	0.004	0.001	0.002	0.001	0.001
Si	0.988	1.008	0.992	0.991	0.946	1.011	1.004	1.003	1.003	1.006	1.002	0.999	1.004
P	0.018	0.013	0.017	0.018	0.006	0.002	0.005	0.003	0.005	0.003	0.004	0.002	0.003
Tot. (B site)	1.006	1.021	1.009	1.009	0.953	1.013	1.009	1.005	1.007	1.009	1.006	1.001	1.006
O	4.000	4.000	4.000	4.000	4.000	4.000	4.000	4.000	4.000	4.000	4.000	4.000	4.000
Cl	-	-	-	-	-	-	-	-	-	-	-	-	-
Tot. (Z site)	4.000	4.000	4.000	4.000	4.000	4.000	4.000	4.000	4.000	4.000	4.000	4.000	4.000

mdl: minimum detection limit. F, La_2O_3, Ce_2O_3, Pr_2O_3, Nd_2O_3, Ho_2O_3, Tm_2O_3 and Lu_2O_3 measured below detection limit. TiO_2 was found to be <mdl in all analyses. * Measured Fe_2O_3 attributed to effects of adjacent hematite and not included in formula calculation or totals. ** Measured MnO (0.05 wt. %), UO_2 (0.04 wt. %), Sm_2O_5 (0.08 wt. %).

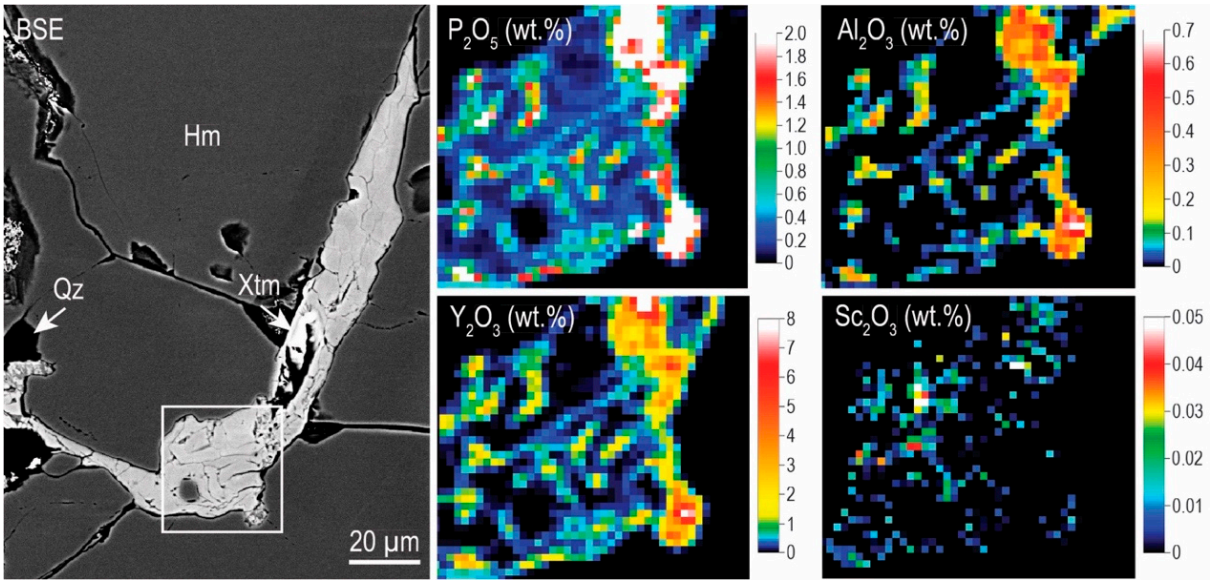

Figure 10. EPMA element map of skeletal zircon from the studied hematite (Hm) ore. The mapped area is shown in the rectangle on the BSE image to the left. Note the presence of the same elements as in the granular zircon (Figure 9). In this case, P, Al and Y show strongest enrichment on one side of the zircon. Despite the low resolution of these images, Sc is nonetheless notable as spots of higher concentration corresponding to patchy areas of enrichment in the other mapped elements. Scales in wt. %.

4.3. Nanoscale Mineral Study

The nanoscale study was carried out for identification of: (i) Zr-rich needles as baddeleyite; and (ii) the core and rim texture in granular zircon mapped in Figure 9.

4.3.1. Baddeleyite

One of the typical fields with inclusions of baddeleyite was selected for the nanoscale study (Figure 11A). Two areas containing needle-like inclusions were assessed by FIB cross-sectioning (Figure 11B–D). Needles present beneath the surface were observed and the presence of two sets of lamellae with orientation at ~110°/70° measured on the surface of the polished block could also be confirmed at depth (Figure 11D).

HAAD-STEM imaging and EDS mapping/spectra of the foil obtained from cut #1 (Figures 11 and 12) show one of the widest (~60 nm) and longest (~3 µm) needles that were identified as baddeleyite, the monoclinic polymorph of ZrO_2. High-resolution imaging was performed with the sample tilted on the $[2\bar{2}.1]$ zone axis in hematite. Baddeleyite and host hematite are crystallographically oriented along lattice directions with ~3.7 Å repeats in each case, i.e., $(011)_{baddeleyite}$ parallel to $(10.\bar{2})_{hematite}$ (Figure 12B–D). In closer detail, stepwise defects are observed to occur that adjust the ~2° misfit between the lattice vectors (012)^(10.-2)~86° and (100)^(011)~84° on $[2\bar{2}.1]_{hematite}$ and $[0\bar{1}1]_{baddeleyite}$ zone axes, respectively (Figure 12D). The bright dots on the atomic-scale images correspond to Fe and Zr atoms in hematite and baddeleyite, respectively, with stacking corresponding to crystal structure models on each respective zone axis (Figure 12E,F).

STEM-EDS element maps of baddeleyite show the major elements Zr and O, with minor Hf and trace concentrations of Si, U and Ti, confirming that the chemistry of the nm-scale Zr-bearing phase in hematite as ZrO_2 (Figure 13A). Relative variation in major and trace elements between the needle and host hematite is shown on the EDS profiles (Figure 13B). We note the relatively high concentration of Ti in baddeleyite (monoclinic) relative to hematite (rhombohedral) (Figure 13C), inferring preferential partitioning during needle crystallization. Titanium affinity for monoclinic ZrO_2 (so-called baddeleyite-TiO_2) has been documented from synthetic studies at the nanoscale [41].

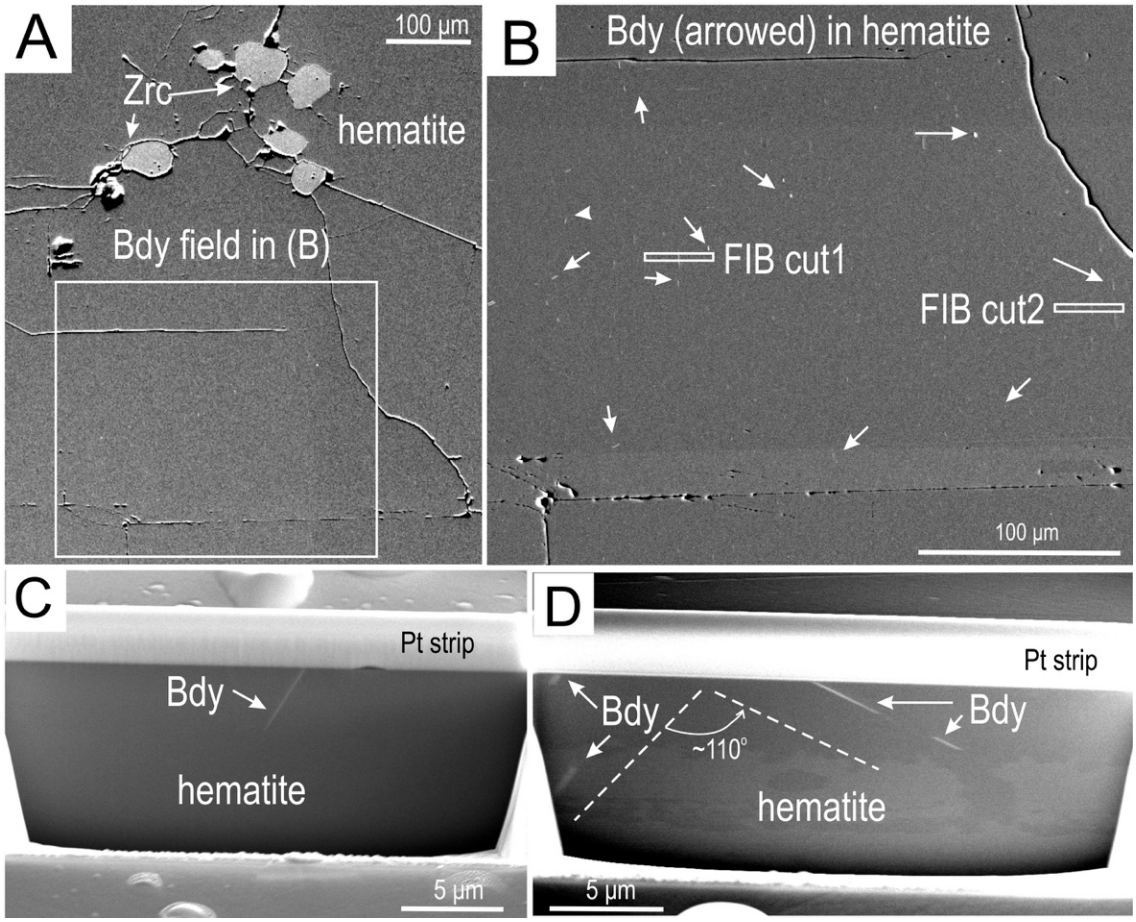

Figure 11. Secondary electron (SE) images showing the field of baddeleyite (Bdy) inclusions in hematite that was sampled for nanoscale analysis after cross-section imaging by FIB-SEM prior to foil preparation for TEM. (**A**) Location of inclusion field adjacent to a cluster of granular zircon (Zrc). (**B**) Location of the two FIB cuts across Bdy inclusions. Note that FIB cut #2 is closer to a fracture. (**C**,**D**) Cross section images of the two FIB cuts in (**B**) showing the Bdy needles and their relative orientations at depth. Note that more needles are aligned along two directions in cut #2, closer to the fracture, and also that the orientation of these needles is different at depth and in FIB cut #2.

4.3.2. Zircon

A second foil, obtained from one of the granular zircon grains was prepared from a slice cut across the core to rim boundary (Figure 14A,B). Imaging of the foil in both BF and HAADF-STEM modes does not show this boundary, even though a number of spotty trails and streaks are present, more abundant within the core than the rim (Figure 14C). No lattice defects or other structural changes could be identified by imaging and no chemical difference could be detected by STEM-EDS spot analysis or mapping. It is most likely that the intensity variation observed on both the BF and HAADF-STEM images is due to cumulative effects of trace element contents, even if the concentrations of individual elements are below the detection limit of the detectors. High-resolution imaging was performed with the specimen tilted on the [001] zone axis in zircon (Figure 14D,E). The core and rim domains are parts of the same grain (single crystal with the same orientation throughout the foil) and the zircon lattice is generally free of defects. Bright spots on the HAADF-STEM images correspond to positions of overlapping Zr and Si atoms on the [001] zone axis in zircon (Figure 14D).

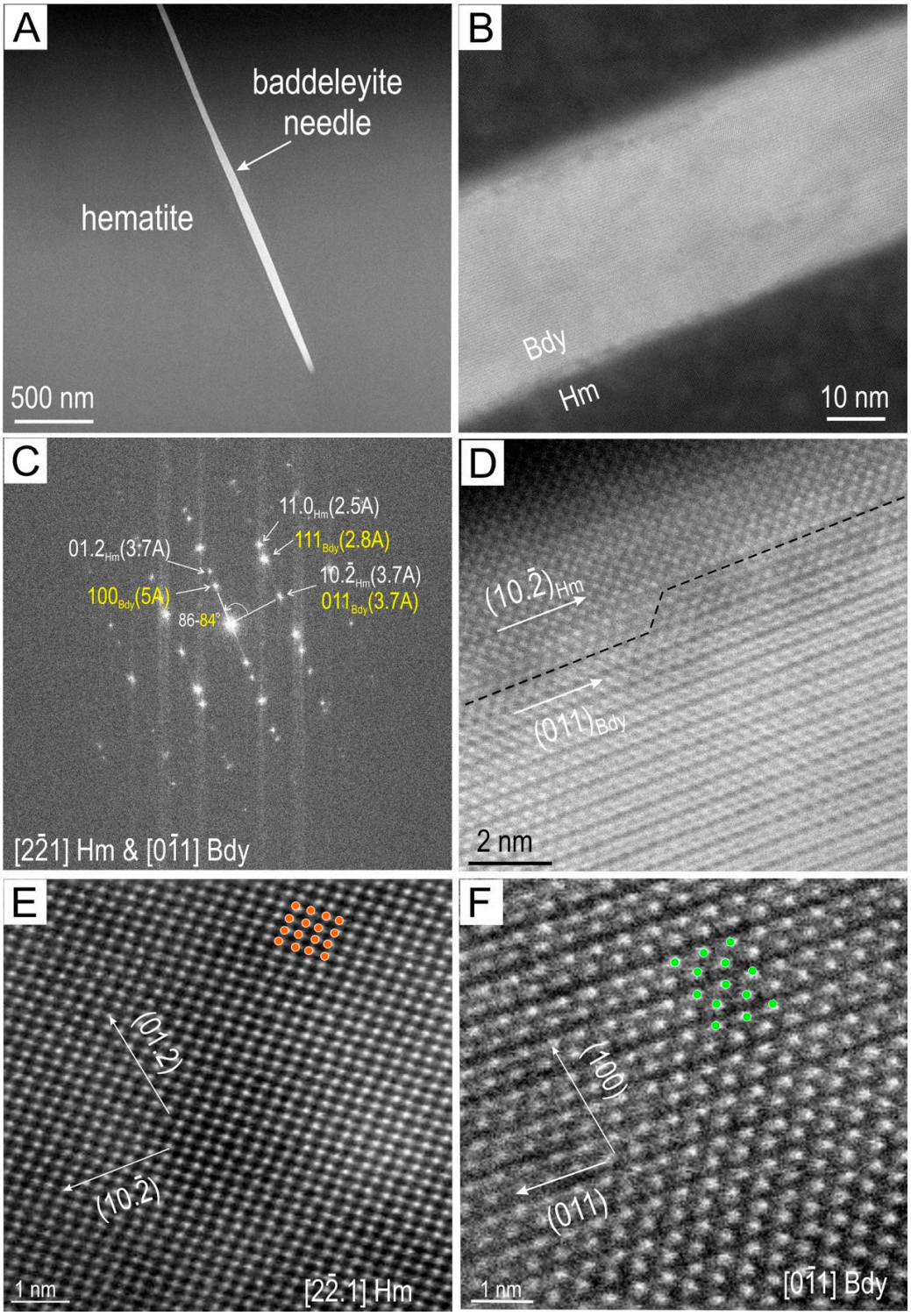

Figure 12. HAADF-STEM images showing baddeleyite (Bdy) in hematite (Hm). (**A**,**B**) Low- and higher-magnification images of Bdy needle (~60 nm-wide; ~3 μm long) within Hm. (**C**) Indexed Fast Fourier Transform (FFT) obtained from image in (**B**) showing the orientation between the two phases on zone axes as marked. (**D**) Coherent orientation between the Bdy on [01$\bar{1}$] zone axis and host Hm on [2$\bar{2}$.1] zone axis. The two lattice vectors with parallel orientation are marked. Note, however, the stepwise defect (dashed line) at the immediate contact between the two minerals. (**E**,**F**) High-resolution images showing distribution of Fe (red) and Zr (green) in Hm and Bdy, respectively, on zone axes as marked. Arrangement of atoms (bright spots) correspond to crystal structure models for the zone axis in each mineral as marked.

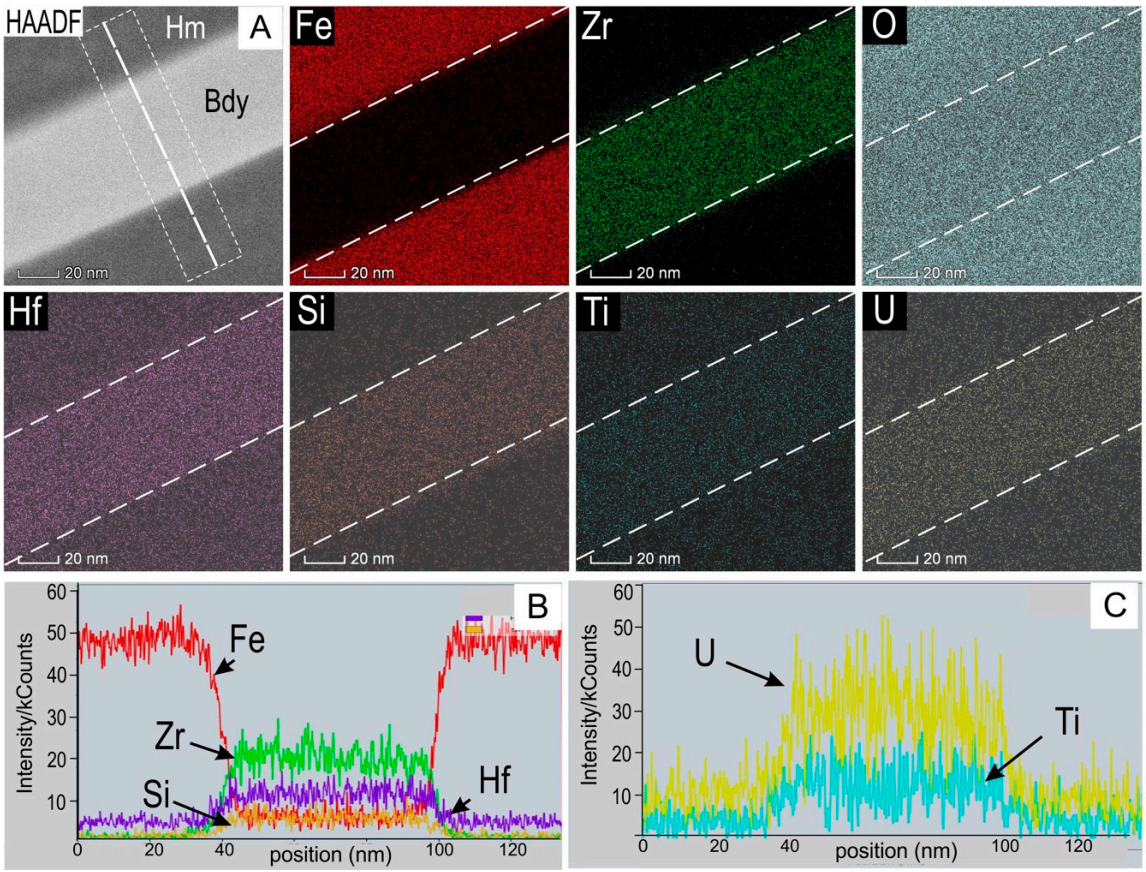

Figure 13. (**A**) HAADF-STEM image and EDS element maps of baddeleyite in host hematite. Elements shown as atom.%. Note that Si is present only in trace amounts. (**B**) Element variation along the profile (dashed line) shown in (**A**). (**C**) Uranium and Ti variation along the same profile in (**B**).

STEM-EDS element mapping shows a relative enrichment in Sc within the grain core (Figure 15A) but no direct correlation between chemistry and the bright streaks/spots on the HAADF image. A profile across the mapped area also shows notable Y, and interestingly, the contact between the rim and core domains is marked by an increase in Y and less pronounced increase in Sc concentration over a distance of 1 μm (Figure 15B). This information complements other data about the distinct chemistry of the core and rim zones, the rims appearing depleted in P on EPMA maps, and are seen to be enriched in U on BSE and CL images (Figure 9). Such chemical variation suggests that the core and rim domains in granular zircon result from an overprint event traceable down to the nanoscale rather than primary growth.

4.4. U–Pb SHRIMP Zircon Geochronology

Cathodoluminescence imaging of zircon aggregates interstitial to hematite and displaying rounded textures shows that the grains lack oscillatory growth zonation typical of magmatic zircon. The grains instead feature core-rim relationships more representative of hydrothermal growth (Figure 16 and Supplementary Figure S1).

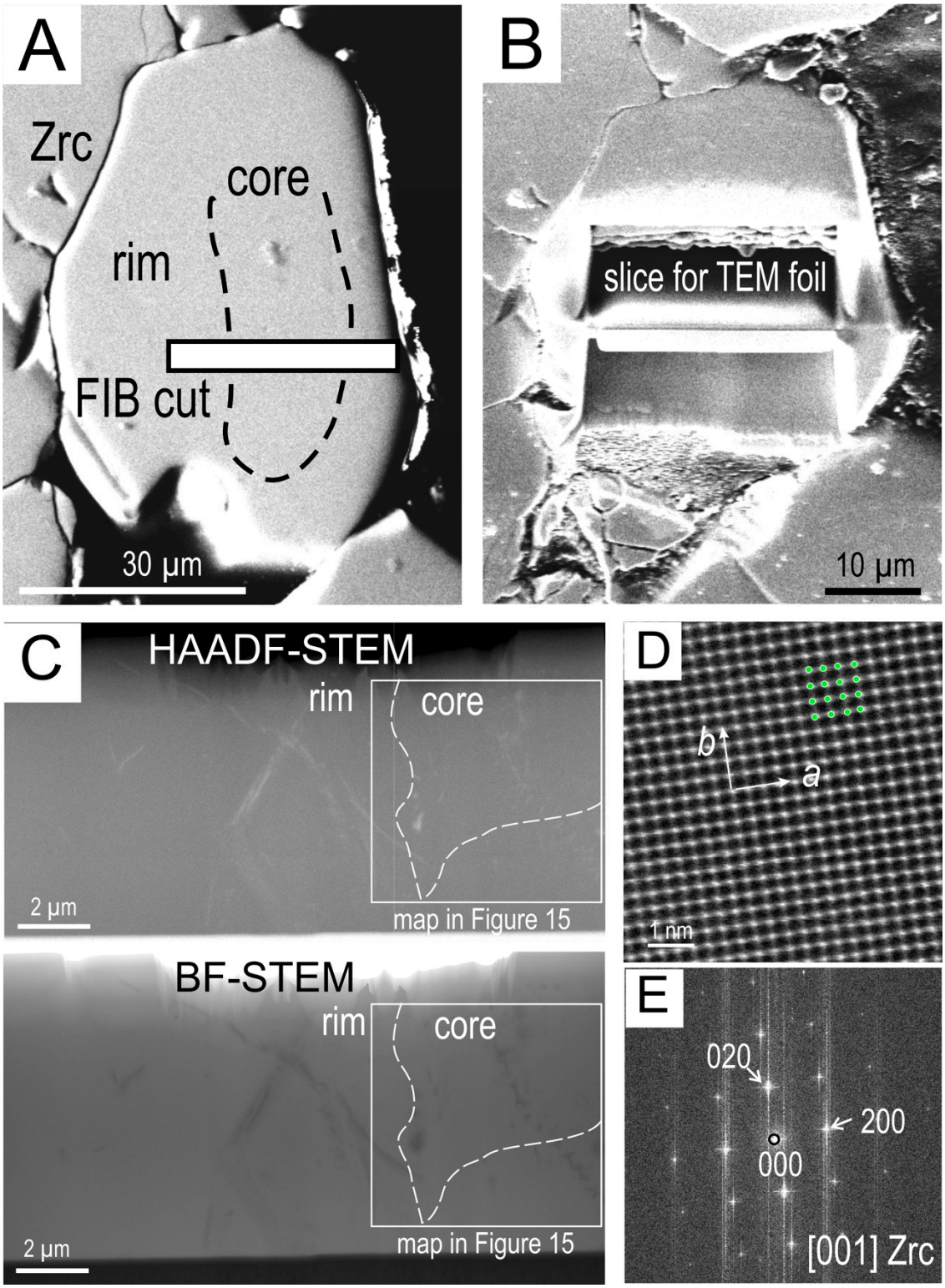

Figure 14. (**A**,**B**) SE images showing location of FIB cut and slice obtained across core and rim of granular zircon (Zrc). (**C**) Bright Field (BF)- and HAADF-STEM images of zircon foil. (**D**) High resolution image of Zrc on [001] zone axis and corresponding indexed FFT in (**E**). The bright spots represent Zr + Si atoms (green circles) with arrangement corresponding to crystal structure model on [001] zone axis in Zrc.

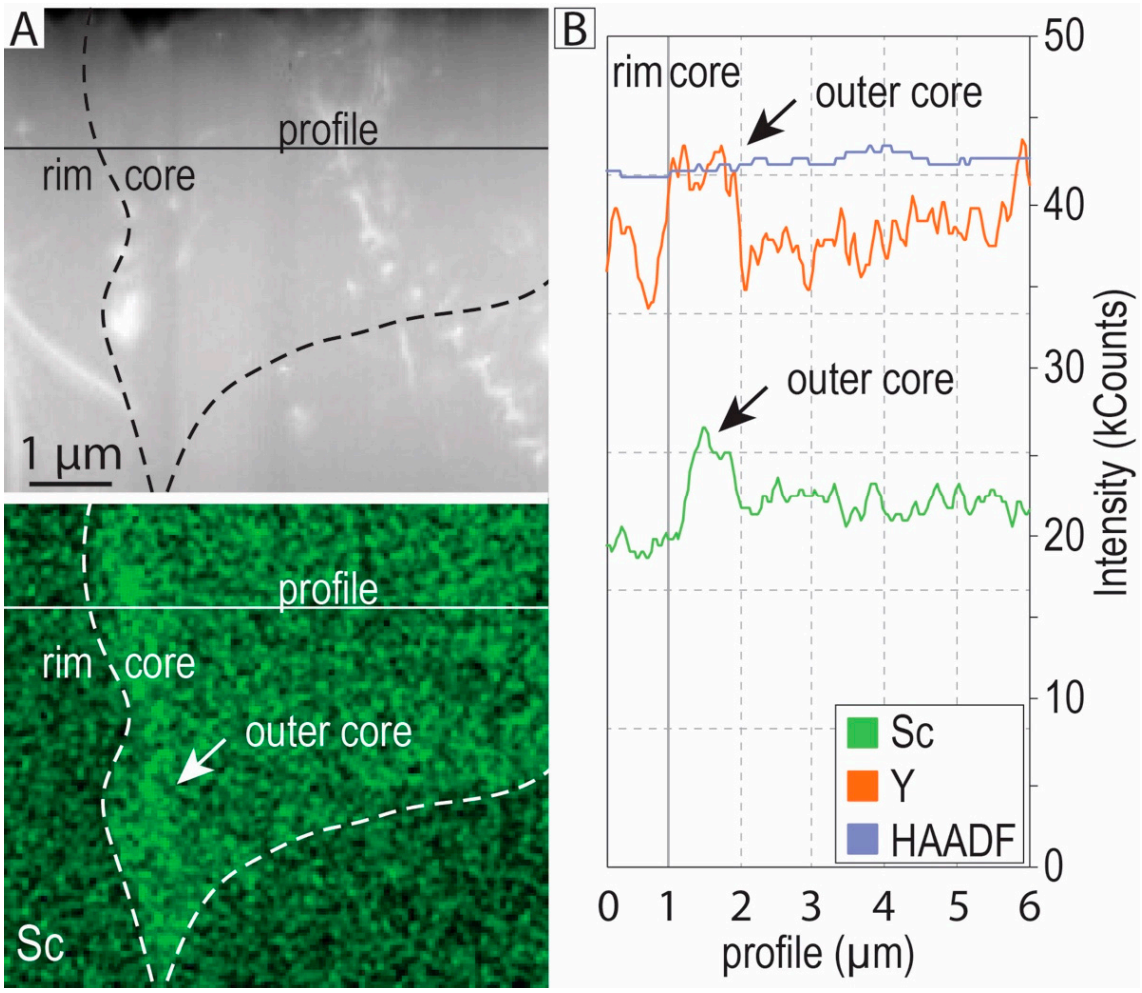

Figure 15. (**A**) HAADF-STEM image and EDS map for Sc (wt. %) in zircon, showing an area across core to rim domains. Note the lack of correlation between bright features in the top image and Sc distribution in the lower image. (**B**) Profile across the boundary between core and rim as marked in (**A**) showing variation in Sc and Y. Note that the contact between the two domains is depicted by a ~1 µm-wide zone enriched in Y and to a lesser extent, also Sc.

Eight spot analyses were collected from the zircon grains. A single grain contained high U (25 ppm), low Th (4.3 ppm), and large discordance (300%) and was not considered for further calculation. Another two grains had $^{206}Pb/^{238}U$ ratios <0.3 and were also not considered further. The remaining five analyses contained low concentrations of U and Th (from ~2–3.5 ppm and ~7–27 ppm, respectively; Table 4). One analysis is reversely discordant (−13) while the remaining four had discordance ranging from 6 to 32%. When anchored to a common-Pb upper intercept at 4500 ± 50 Ma, the data form a discordia line with a lower intercept age of 1731 ± 50 Ma (MSWD = 0.024). A $^{206}Pb/^{238}U$ weighted mean age was used due to the presence of common-Pb affecting the $^{207}Pb/^{206}Pb$ weighted mean and yielding an artificially old age. The three most concordant grains were used to obtain a $^{206}Pb/^{238}U$ weighted mean age of 1741 ± 49 Ma (MSWD = 0.86), which is interpreted to reflect the timing of zircon formation.

Table 4. U, Th and Pb isotope data.

							Age							Isotopic Ratio						
	%	U	Th	^{206}Pb *	^{232}Th		^{206}Pb		^{207}Pb		^{208}Pb		%	^{207}Pb *		^{207}Pb *		^{206}Pb *		Err
#	^{206}Pbc	ppm	ppm	ppm	/^{238}U	±%	/^{238}U	±1σ	/^{206}Pb	±1σ	/^{232}Th	±1σ	Disc.	/^{206}Pb *	±%	/^{235}U	±%	/^{238}U	±%	Corr
1	−1.54	3.2	7	0.84	2.3	1.99	1717	105	1805	253	1883	175	6	0.110	14	4.64	16	0.305	6.9	0.4
2	1.92	6.8	18	1.8	2.7	2.92	1720	74	1538	292	1512	109	−13	0.096	16	4.03	16	0.306	4.9	0.3
3	−2.03	2.4	11	0.68	4.6	2.25	1809	128	2186	250	1850	233	20	0.137	14	6.11	17	0.324	8.1	0.5
4	2.37	7.3	23	1.6	3.2	1.30	1449	63	1183	335	1376	90	−25	0.079	17	2.76	18	0.252	4.9	0.3
5	−2.58	12	34	2.7	3.0	2.62	1537	87	1843	265	1624	140	19	0.113	15	4.18	16	0.269	6.3	0.4
6	−2.23	7.5	21	2.1	3.0	1.63	1790	89	2103	201	1938	173	17	0.130	11	5.75	13	0.320	5.7	0.4
7	−3.44	1.8	27	0.52	15	5.43	1842	171	2545	543	1514	186	32	0.169	32	7.69	34	0.331	11	0.3

* Common Pb corrected using measured ^{204}Pb.

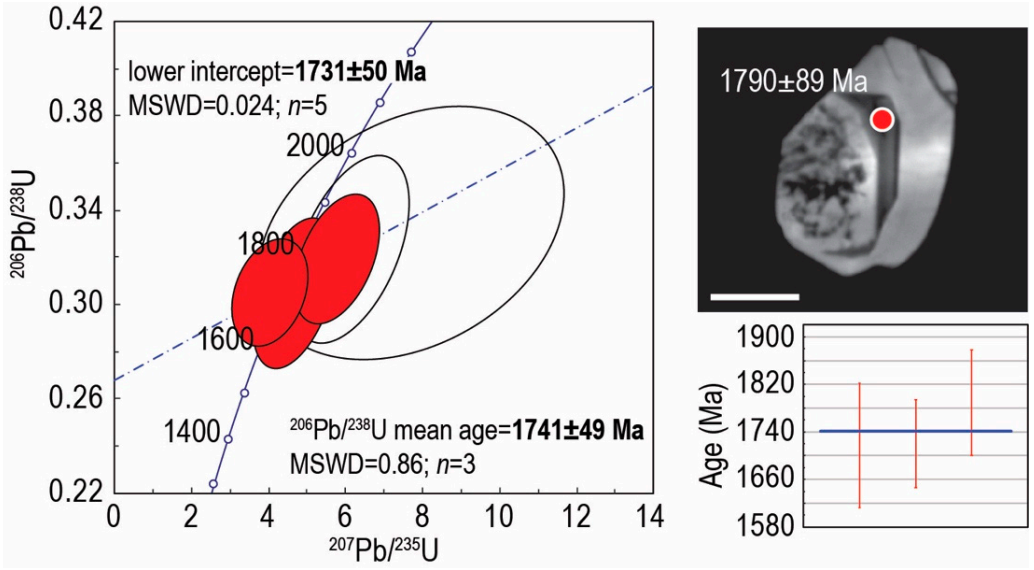

Figure 16. Concordia diagram presenting SHRIMP U–Pb data for zircon along with a CL image of a representative zircon grain and its respective ^{206}Pb/^{238}U age. Zircon grains used for a ^{206}Pb/^{238}U weighted mean age are colored red.

5. Discussion

5.1. Recognition of Metamorphic Textures

Hematite displays textures attributable to annealing under conditions of high-grade metamorphism, e.g., 120° triple junction "foam" textures comparable with those observed in many metamorphosed massive pyrite ores [42]. This is concordant with an interpretation in which the Peculiar Knob ore underwent metamorphism at $T > 680$ °C based on the thermoremanent magnetization history of comparable coarse hematite [12]. Although no fine-scale lamellar microstructure is observed in samples studied here, the presence of twins and tiny inclusions of magnetite are common features of the coarse hematite at Peculiar Knob and are analogous to those reported by Schmidt et al. [12]. In addition, we show that, although no metamorphic silicates are present, the gangue minerals also exhibit fabrics indicative of metamorphism, e.g., rotational patterns within quartz, or imbricate intergrowths between siderite and quartz. Nonetheless, superimposed textures in hematite, including decussate boundaries, microfractures, pressure gashes, porosity are evidence for deformation associated with fluid percolation during retrograde metamorphism or to a later tectono-magmatic event.

This is the first report of high Zr (hundreds of ppm) and Ti (1,500 ppm) concentrations in hematite from Peculiar Knob. We show that only Ti can be inferred as lattice-bound, whereas sub-µm inclusions of baddeleyite can account for the Zr content as measured by LA-ICP-MS. Formation of such Zr- and Ti-bearing hematite cannot be reconciled with chemical precipitation alone in a BIF environment, as had been previously considered (e.g., [10]).

5.2. Bridging Micron- to Nanoscale Observations in Hematite: Reconstruction of Ore Evolution

Nanoscale twinning has been shown in hematite grown from acicular goethite [43], a mechanism we consider feasible during diagenesis. Nonetheless, the studied hematite is markedly coarse-grained and the twinning is most likely related to syn-metamorphic deformation, in which case accommodation of strain takes place along glide planes ([44], and references therein). The ~85° angle between twins and crystal elongation in some hematite grains (Figure 3b) is comparable to the 84–86° angle between the reciprocal lattice vectors in epitaxial intergrowths of baddeleyite and hematite, i.e., $(011)^*_{\text{baddeleyite}}$ II $(10.\bar{2})^*_{\text{hematite}}$ and $(100)^*_{\text{baddeleyite}}$ II $(01.2)^*_{\text{hematite}}$ (Figure 12). Rhombohedral ("*r*") type twins in metamorphosed hematite were measured relative to the parent crystal by a rotation of 85° about the $r = (02\bar{2}1)$ direction [44], equivalent to the $(01\bar{1}2)^*$ direction in reciprocal space (indicated as $(01.2)^*$ on Figure 12C). This implies that twinning in hematite can be correlated with the fine adjustment of epitaxial intergrowths with baddeleyite during the same syn-deformational metamorphic event.

On the other hand, the angle between baddeleyite needles is distinct, by ~15°, from the "r" twin angle discussed above, with conjugate set of needles at ~110°/70° (Figure 4A–C and Figure 11D). These values correspond to the obtuse/acute angles between $(111)\hat{}(1\bar{1}\bar{1})$ and $(\bar{1}\bar{1}\bar{1})\hat{}(\bar{1}1\bar{1})$ pairs of lattice vectors, respectively, in magnetite, and such crystallographic directions are often marked by trellis exsolutions formed during cooling of titanomagnetite (Ti–Mt) (e.g., [45], and references therein). The 15° offset is observed between the crystal orientations of some relict magnetite grains relative to the twin planes in hematite in which they are located (Figure 3F). Whereas relict magnetite can be preserved within hematite, the two minerals share equilibrium boundaries on $fO_2 - fS_2$ phase diagrams over temperature ranges of many geological environments, ilmenite is not stable with hematite. However, knowing that ilmenite is a good host for Zr relative to magnetite [46], decomposition of ilmenite could have led to: (i) exsolutions of baddeleyite within magnetite undergoing transformation into hematite; and (ii) subsequent relative enrichment of Ti in that hematite.

5.3. Zirconium Mineralogy: Geological Evolution at Peculiar Knob

Metamorphic differentiation can lead to migmatite formation, thus accounting for segregation of mafic and felsic minerals in a pre-existing lithology via sub-solidus remobilization and/or partial melting. For example, based on zircon geochronology indicating the presence of detrital zircon, the Warramboo

magnetite gneisses in the southeastern Gawler Craton, which was previously considered an Archean BIF, has been reinterpreted as a package of Fe-rich sediments that underwent deformation and granulite facies metamorphism during the Kimban Orogeny [47]. An increase in Fe content and the large-scale structural architecture of the Warramboo deposit was ascribed to melt loss and deformation during metamorphism. Such a process of iron-oxide concentration is, however, unlikely, by itself, to explain formation of hematite-rich orebodies at Peculiar Knob considering their high-grade, deposit size and the absence of metamorphic silicates (pyroxene, amphibole, garnet, etc.) at least not in the studied ore, among other arguments.

A potential source for the hematite protore could therefore be detrital titanomagnetite sourced from mafic/ultramafic rocks and deposited within a sedimentary basin. Such heavy mineral horizons could have been of sufficient volume to have formed an Fe-rich sediment with or without chemical precipitates. This hypothesis would also explain the Cr concentrations in hematite. A diagenesis-uplift cycle typical of Fe-rich sediment packages of this type could have led to transformation of magnetite into martite (pseudomorphic replacement of magnetite by hematite) with subsequent granoblastic coarsening and annealing during a high-grade metamorphic event such as the Kimban Orogeny. Ilmenite has been recognized as an important source of Zr during granulite facies metamorphism and baddeleyite associated with magmatic ilmenite in mafic granulites was interpreted as an exsolution product [48]. This infers that, ilmenite, although no longer present, may have been the source of Zr in the studied hematite. The age yielded by U–Pb SHRIMP analysis of zircon reported here, although not well constrained (1741 ± 49 Ma), is nevertheless similar to the age reported for the Kimban Orogeny with peak metamorphism at granulite facies (1736 ± 14 Ma; [24]).

The zircon cannot be readily linked to formation of baddeleyite in the same sample given the lack of similarity in the geochemical signature between the two Zr-minerals (e.g., Ti in baddeleyite, Sc in zircon), difference in both size and grain morphology, as well as lack of any observable relationships between the two minerals. A detrital origin was considered for Sc-bearing zircon found in association with pretulite ($ScPO_4$) and xenotime-(Y) in an Ordovician apatite-rich, oolitic ironstone from the Armorican Massif, France [49]. Low-temperature, P-bearing hydrothermal fluids were considered responsible for mineral reactions leading to Zr remobilization to form the Sc-phosphate during diagenesis and low-grade metamorphism. Scandium-rich zircon was also reported from xenotime-rich veins attributed to percolation of acidic, volatile-rich fluids, possibly granite-derived, through porous arkose units in the Browns Ranges REE deposit, Western Australia [50].

Although detrital zircon from a granitic source is an option, both the metamorphic age obtained, and the very low U concentrations represent arguments against a granitic source. Nonetheless, the association between Sc and P, as well as the inclusions of fluorapatite within the zircon cores (Figure 9) could be indicative of comparable low-T, P- and Si-bearing, acidic fluids that could have locally interacted with inclusions of ilmenite/baddeleyite within the titanomagnetite at the time of martitization, producing the observed Sc-bearing cores in the granular zircon. Scandium could have been remobilized by such fluids from the same Fe-Ti-oxides, since magmatic ilmenite can carry tens of ppm Sc (e.g., [7]). Baddeleyite can also be converted to zircon as a result of increased silica activity [51]. Recent assessment of the P-T conditions controlling zircon behavior during metamorphism indicates that growth occurs during late-stage exhumation/cooling, whereas prograde metamorphism is responsible for zircon dissolution ([52], and references therein). Therefore, growth of the granular zircon with Sc-P-Al-bearing cores during uplift could have been followed by zircon partial dissolution resulting in the skeletal zircon, locally preserving granular morphology with Sc-bearing domains preserved (Figure 10).

The distinct Sc-free rims in zircon with a narrow Sc- and Y-rich boundary depicted at the nanoscale (Figure 11B), are attributable to later fluid percolation, possibly associated with granite-derived hydrothermal fluids associated with the ~1.6 Ga Hiltaba Suite intrusions intersected in drillholes at depth beneath the deposit (Figure 1A). The modest recrystallization along the margins of hematite

grains, featuring a conspicuous Sn–W–Nb–Sb trace element signature is consistent with hydrothermal overprinting associated with Hiltaba magmatism [5,53].

6. Conclusions and Implications

The measured Zr concentration in hematite of average ~260 ppm is directly attributable to nm-scale inclusions of baddeleyite. These are likely pervasively distributed throughout the sample based on the inclusions observed beneath the surface and with smaller size. A distinction between such nm-scale inclusions and lattice-bound trace element substitutions cannot be made from LA-ICP-MS data alone and can only confirmed by nanoscale sample characterization [54].

The evidence presented here suggests that multiple events contributed to formation of the massive orebody at Peculiar Knob. Detrital titanomagnetite is considered to have been a source for Zr, Ti, Cr and Sc in a sedimentary environment via erosion of mafic rocks. The Fe-rich sedimentary package underwent diagenesis, followed by uplift and supergene ore enrichment leading to desilicification, compaction and martitization. This was followed by subsequent burial, deformation and high-grade metamorphism during the Kimban Orogeny. Later interaction with Hiltaba granitoids and distal hydrothermal fluids associated with those granites, led to W, Sn and Sb enrichment in hematite.

Zirconium mineralogy and geochemistry, the presence and distribution of Zr in iron-oxides and of Sc in zircon could represent potential indicators of ore formation. Similar characteristics might be anticipated in other Fe-rich prospects in South Australia and elsewhere. This study further demonstrates that observations bridging the micron- to nanoscales, using complimentary advanced microanalytical techniques, can provide critical constraints on ore-forming processes [12].

Supplementary Materials: The following are available online at http://www.mdpi.com/2075-163X/9/4/244/s1, Supplementary Material A: Details of analytical Methods; Figure S1, Cathodoluminescence images of zircon grains. References [55–64] are cited in the supplementary materials.

Author Contributions: W.K. and C.L.C. conceived this contribution and conducted all analytical work, assisted by A.S. with operating the Titan Themis instrument and B.P.W. with EPMA set-up. H.F. and G.J. provided the sample and unpublished background information on Peculiar Knob. The manuscript was written by W.K., C.L.C. and N.J.C., with contributions from K.E., B.P.W., H.F., G.J., and A.S.

Funding: This research is a contribution to the project "Trace elements in iron-oxides: deportment, distribution and application in ore genesis, geochronology, exploration and mineral processing", supported by BHP Olympic Dam and the South Australian Government Mining and Petroleum Services Centre of Excellence. N.J.C. acknowledges additional support from the ARC Research Hub for Australian Copper-Uranium (Gran IH130200033).

Acknowledgments: The authors acknowledge the facilities, and the scientific and technical assistance, of the Microscopy Australia node, Adelaide Microscopy at The University of Adelaide. Logistical support from site geologists at Southern Iron is greatly appreciated. Allen Kennedy is thanked for assistance with SHRIMP operation. Wenyuan Liu and Animesh Basak assisted with FIB operation. Sarah Gilbert assisted with LA-ICP-MS analysis. We gratefully acknowledge the helpful comments of two *Minerals* reviewers.

Conflicts of Interest: The authors declare no conflicts of interest.

References

1. Dawson, J.B.; Steele, I.M.; Smith, J.V.; Rivers, M.L. Minor and trace element chemistry of carbonates, apatites and magnetites in some African carbonatites. *Mineral. Mag.* **1996**, *60*, 415–425. [CrossRef]
2. Reguir, E.P.; Chakhmouradian, A.R.; Halden, N.M.; Yang, P.; Zaitsev, A.N. Early magmatic and reaction-induced trends in magnetite from the carbonatites of Kerimasi, Tanzania. *Can. Mineral.* **2008**, *46*, 879–900. [CrossRef]
3. Selmi, M.; Lagoeiro, L.E.; Endo, I. Geochemistry of hematite and itabirite, Quadrilátero Ferrífero, Brazil. *Revista Escola de Minas* **2009**, *62*, 35–43. [CrossRef]
4. Cabral, A.R.; Rosière, C.A. The chemical composition of specular hematite from Tilkerode, Marz, Germany: Implications for the genesis of hydrothermal hematite and comparison with the Quadrilátero Ferrífero of Minas Gerais, Brazil. *Mineral. Depos.* **2013**, *48*, 907–924. [CrossRef]

5. Verdugo-Ihl, M.R.; Ciobanu, C.L.; Cook, N.J.; Ehrig, K.; Courtney-Davies, L.; Gilbert, S. Textures and U-W-Sn-Mo signatures in hematite from the Cu-U-Au-Ag orebody at Olympic Dam, South Australia: Defining the archetype for IOCG deposits. *Ore Geol. Rev.* **2017**, *91*, 173–195. [CrossRef]
6. Keyser, W.M.; Ciobanu, C.L.; Cook, N.J.; Johnson, G.; Feltus, F.; Johnson, S.; Dmitrijeva, M.; Ehrig, K.; Nguyen, P. Petrography and trace element signatures of iron-oxides in deposits from the Middleback Ranges, South Australia: From banded iron formation to ore. *Ore Geol. Rev.* **2018**, *93*, 337–360. [CrossRef]
7. Gao, W.; Ciobanu, C.L.; Cook, N.J.; Huang, F.; Mang, L.; Gao, S. Petrography and trace element signatures in silicates and Fe-Ti-oxides from the Lanjiahuoshan deposit, Panzhihua layered intrusion, Southwest China. *Lithos* **2017**, *294–295*, 164–183. [CrossRef]
8. Jones, T.S.; Kimura, S.I.; Muan, A. Phase relations in the system FeO–Fe_2O_3–ZrO_2–SiO_2. *J. Am. Ceram. Soc.* **1967**, *50*, 137–142. [CrossRef]
9. Bechta, S.V.; Krushinov, E.V.; Al'myashev, V.I.; Vitol, S.A.; Mezentseva, L.P.; Petrov, Y.B.; Lopukh, D.B.; Khabenskii, V.B.; Barrachin, M.; Hellmann, S.; et al. Phase relations in the ZrO_2–FeO system. *Russian J. Inorg. Chem.* **2006**, *51*, 325–331.
10. Morris, B.J.; Hough, J.K. *South Australia Steel and Energy Project, Peculiar Knob Prospect, South Australia*; Department of Mines and Energy Resources Report Book 97/9; Department of Primary Industries & Resources: Adelaide, Australia, 1997.
11. Nielson, S. *Peculiar Knob Resource Model Development*; Arrium Mining: Adelaide, Australia, 2014; 55p.
12. Schmidt, P.W.; McEnroe, S.A.; Clark, D.A.; Robinson, P. Magnetic properties and potential field modeling of the Peculiar Knob metamorphosed iron formation, South Australia: An analog for the source of the intense Martian magnetic anomalies? *J. Geophys. Res.* **2007**, *112*, B03102. [CrossRef]
13. Ciobanu, C.L.; Cook, N.J.; Maunders, C.; Wade, B.P.; Ehrig, K. Focused Ion Beam and Advanced Electron Microscopy for Minerals: Insights and Outlook from Bismuth Sulphosalts. *Minerals* **2016**, *6*, 112. [CrossRef]
14. Flint, R.B.; Benbow, M.C. *Geology of the Mount Woods Inlier*; Department of Mines, South Australia Report Book 77/134; Department for Energy and Mining: Adelaide, Australia, 1977; 50p.
15. Chalmers, N. *The Mount Woods Domain: A Geological Review and Discussion on Mineralisation Potential*; Department of Primary Industries and Resources Report Book 2007/7; Department of Primary Industries & Resources: Adelaide, Australia, 2007; 62p.
16. Parker, A.J.; Lemon, N.M. Reconstruction of the early Proterozoic stratigraphy of the Gawler Craton, South Australia. *J. Geol. Soc. Aust.* **1982**, *29*, 221–238. [CrossRef]
17. Vassallo, J.J.; Wilson, C.J.L. Structural repetition of the Hutchison Group metasediments, Eyre Peninsula, South Australia. *Aust. J. Earth Sci.* **2001**, *48*, 331–345. [CrossRef]
18. Szpunar, M.; Hand, M.; Barovich, K.; Jagodzinski, E.; Belousova, E. Isotopic and geochemical constraints on the Paleoproterozoic Hutchison Group, southern Australia: Implications for Paleoproterozoic continental reconstructions. *Precambr. Res.* **2011**, *187*, 99–126. [CrossRef]
19. Jagodzinski, E.A. Compilation of SHRIMP U-Pb geochronological data, Olympic Domain, Gawler Craton, South Australia, 2001–2003. *Geosci. Aust. Rec.* **2005**, *20*, 2005.
20. Fanning, C.M. *Ion-Microprobe U–Pb Zircon Dating of the Mount Woods Inlier, Preliminary Results*; Research School of Earth Sciences, Australian National University: Canberra, Australia, 1993; 8p.
21. Skirrow, R.G.; Bastrakov, E.N.; Barovich, K.; Fraser, G.L.; Creaser, R.A.; Fanning, C.M.; Raymond, O.L.; Davidson, G.J. Timing of iron oxide Cu-Au-(U) hydrothermal activity and Nd isotope constraints on metal sources in the Gawler Craton, South Australia. *Econ. Geol.* **2007**, *102*, 1441–1470. [CrossRef]
22. Forbes, C.J.; Giles, D.; Hand, M.; Betts, P.G.; Suzuki, K.; Chalmers, N.; Dutch, R. Using P-T paths to interpret the tectonothermal setting of prograde metamorphism: An example form the northeastern Gawler Craton, South Australia. *Precambr. Res.* **2011**, *185*, 65–85. [CrossRef]
23. Ambrose, G.J.; Flint, R.B. BILLA KALINA, South Australia. Explanatory Notes 250000 geological series Sheet SH/53-7. *Geol. Surv. South Austr.* **1981**, *1*, 36.
24. Fanning, C.M.; Flint, R.B.; Parker, A.J.; Ludwig, K.R.; Blisset, A.H. Refined Preoterozoic evolution of the Gawler Craton, South Australia, through U–Pb zircon geochronology. *Precambr. Res.* **1988**, *40/41*, 363–386. [CrossRef]
25. Finlay, J. Structural Interpretation of the Mount Woods Inlier. Ph.D. Thesis, Monash University, Melbourne, Australia, 1993.
26. Holm, O. New geochronology of the Mount Woods Inlier and the central Gawler gold province. In *Gawler Craton: State of Play 2004*; Report Book; Department of Primary Industries & Resources: Adelaide, Australia, 2004.

27. Jagodzinski, E.A.; Reid, A.J.; Chalmers, N.; Swain, G.; Frew, R.A.; Foudoulis, C. *Compilation of SHRIMP U-Pb Geochronological Data for the Gawler Craton, South Australia*; Department of Primary Industries & Resources Report Book 2007/21; Department of Primary Industries & Resources: Adelaide, Australia, 2007.
28. Belperio, A.; Flint, R.; Freeman, H. Prominent Hill: A hematite-dominated, iron oxide copper-gold system. *Econ. Geol.* **2007**, *102*, 1499–1510. [CrossRef]
29. Betts, P.G.; Valenta, R.K.; Finlay, J. Evolution of the Mount Woods Inlier, northern Gawler Craton, Southern Australia: An integrated structural and aeromagnetic analysis. *Tectonophysics* **2003**, *366*, 83–111. [CrossRef]
30. Davies, M.B. *Iron ore in South Australia*; Commodity Review No. 8; Primary Industries and Resources: Adelaide, Australia, 2000; 35p.
31. Daly, S.J.; Fanning, C.M.; Fairclough, M.C. Tectonic evolution and exploration potential of the Gawler Craton South Australia. *AGSO J. Aust. Geol. Geophys.* **1988**, *17*, 145–168.
32. Reid, A.J.; Fabris, A. Influence of preexisting low metamorphic grade sedimentary successions on the distribution of iron oxide copper-gold mineralization in the Olympic Cu-Au Province, Gawler Craton. *Econ. Geol.* **2015**, *110*, 2147–2157. [CrossRef]
33. Guillong, M.; Hametner, K.; Reusser, E.; Wilson, S.A.; Günther, D. Preliminary characteristics of new glass reference materials (GSA-1G, GSC-1G, GSD-1G and GSE-1G) by laser ablation-inductively coupled plasma-mass spectrometry using 193 nm, 213 nm and 266 nm wavelengths. *Geostand. Geoanal. Res.* **2005**, *29*, 315–331. [CrossRef]
34. Jochum, K.P.; Weis, U.; Stoll, B.; Kuzmin, D.; Yang, Q.; Raczek, I.; Jacob, D.E.; Stracke, A.; Gunther, D.; Enzweiler, J. Determination of reference values for NIST SRM 610-617 glasses following ISO guidelines. *Geostand. Geoanal. Res.* **2011**, *35*, 397–429. [CrossRef]
35. Van Achterbergh, E.; Ryan, C.G.; Jackson, S.E.; Griffin, W.L. Data reduction software for LA-ICP-MS. In *Laser-ablation-ICPMS in the Earth Sciences: Principles and Applications*; Sylvester, P.J., Ed.; Mineralogical Association of Canada: Quebec City, QC, Canada, 2001; pp. 239–243.
36. Woodhead, J.D.; Hellstrom, J.; Paton, C.; Hergt, J.M.; Greig, A.; Maas, R. A guide to depth profiling and imaging applications of LA-ICM-PS. In *Laser Ablation ICP-MS in the Earth Sciences: Current Practices and Outstanding Issues*; Mineralogical Association of Canada, Short Course Series 40; Sylvester, P.J., Ed.; Mineralogical Association of Canada: Quebec City, QC, Canada, 2008; pp. 135–145.
37. Ciobanu, C.L.; Cook, N.J.; Utsunomiya, S.; Pring, A.; Green, L. Focussed ion beam transmission electron microscopy applications in ore mineralogy: Bridging micro and nanoscale observations. *Ore Geol. Rev.* **2011**, *42*, 6–31. [CrossRef]
38. Compston, W.; Williams, I.S.; Meyer, C. U-Pb geochronology of zircon from lunar breccia 73217 using a sensitive high mass-resolution ion microprobe. *J. Geophys. Res.* **1984**, *89*, 525–534. [CrossRef]
39. Williams, I.S. U–Th–Pb geochronology by ion microprobe. In *Applications of Microanalytical Techniques to Understanding Mineralizing Processes*; McKibben, M.A., Shanks, W.C., Eds.; Society of Economic Geologists: Littleton, CO, USA, 1998; Volume 7, pp. 1–35.
40. McDonough, W.F.; Sun, S.S. Composition of the Earth. *Chem. Geol.* **1995**, *120*, 223–253. [CrossRef]
41. Swamy, V.; Dubrovinsky, L.S.; Dubrovinskaia, N.A.; Langenhorst, F.; Simionovici, A.S.; Drakopoulos, M.; Dmitriev, V.; Weber, H.-P. Size effects on the structure and phase transition behavior of baddeleyite TiO_2. *Solid State Commun.* **2005**, *134*, 541–546. [CrossRef]
42. Craig, J.R.; Vaughan, D.J. *Ore Microscopy and Ore Petrography*, 2nd ed.; John Wiley & Sons: Hoboken, NJ, USA, 1994.
43. Löffler, L.; Mader, W. Anisotropic X-ray peak broadening and twin formation in hematite derived from natural and synthetic goethite. *J. Eur. Ceram. Soc.* **2006**, *26*, 131–139. [CrossRef]
44. Avila, C.F.; Lagoeiro, L.; Barbosa, P.F.; Graca, L. EBSD analysis of rhombohedral twinning in hematite crystals of naturally deformed iron formations. *J. Appl. Crystallogr.* **2015**, *48*, 212–219. [CrossRef]
45. Gao, W.; Ciobanu, C.L.; Cook, N.J.; Slattery, A.; Huang, F.; Wang, D. Nanoscale study of lamellar exsolutions in clinopyroxene from olivine gabbro: Recording crystallization sequences in iron-rich layered intrusions. *Am. Mineral.* **2018**, *104*, 244–261.
46. Morisset, C.; Scoates, J.S.; Weis, D.A. Partitioning of trace elements during exsolution in ilmenite-hematite series minerals by LA-ICP-MS. In Proceedings of the AGU Fall Meeting Abstracts, San Francisco, CA, USA, 12–16 December 2010.

47. Lane, K.; Jagodzinski, E.A.; Dutch, R.; Reid, A.J.; Hand, M. Age constraints on the timing of iron ore mineralisation in the southeastern Gawler Craton. *Aust. J. Earth Sci.* **2015**, *62*, 55–75. [CrossRef]
48. Bingen, B.; Austrheim, H.; Whitehouse, M. Ilmenite as a source for zirconium during high-grade metamorphism? Textural evidence from the Caledonides of western Norway and implications for zircon geochronology. *J. Petrol.* **2001**, *42*, 355–375. [CrossRef]
49. Moëlo, Y.; Lulzac, Y.; Rouer, O.; Palvadeau, P.; Gloaguen, É.; Léone, P. Scandium mineralogy: Pretulite with scandian zircon and xenotime-(Y) within an apatite-rich oolitic ironstone from Saint-Aubin-des-Châteaux, Armorican Massif, France. *Can. Mineral.* **2002**, *40*, 1657–1673. [CrossRef]
50. Cook, N.J.; Ciobanu, C.L.; O'Reilly, D.; Wilson, R.; Das, K.; Wade, B. Mineral chemistry of rare earth element (REE) mineralization, Browns Range, Western Australia. *Lithos* **2013**, *172*, 192–213. [CrossRef]
51. Harley, S.L.; Kelly, N.M.; Möller, A. Zircon behavior and the thermal histories of mountain chains. *Elements* **2007**, *3*, 25–30. [CrossRef]
52. Kohn, M.J.; Corrie, S.L.; Markley, C. The fall and rise of metamorphic zircon. *Am. Mineral.* **2015**, *100*, 897–908. [CrossRef]
53. Keyser, W.M.; Ciobanu, C.L.; Cook, N.J.; Courtney-Davies, L.; Ehrig, K.; Gilbert, S.; McPhie, J. Links between sedimentary protoliths and IOCG Links between sedimentary protoliths and IOCG-skarn skarn alteration, Island Dam, South Australia. In Proceedings of the 14th SGA Biennial Meeting, Quebec City, QC, Canada, 20–23 August 2017; pp. 935–938.
54. Cook, N.J.; Ciobanu, C.L.; George, L.; Zhu, Z.-Y.; Wade, B.; Ehrig, K. Trace Element Analysis of Minerals in Magmatic-Hydrothermal Ores by Laser Ablation Inductively-Coupled Plasma Mass Spectrometry: Approaches and Opportunities. *Minerals* **2016**, *6*, 111. [CrossRef]
55. Ludwig, K.R.A. *SQUID*, version 2.50; Special Publication No. 5; A User's Manual; Berkeley Geochronology Center: Berkeley, CA, USA, 2009; p. 110.
56. Steiger, R.H.; Jäger, E. Subcommission of geochronology: Convention on the use of decay constants in geo- and cosmochronology. *Earth Plan. Sci. Lett.* **1977**, *36*, 359–362. [CrossRef]
57. Armstrong, J.T. Quantitative analysis of silicate and oxide minerals: Comparison of Monte Carlo, ZAF, and φ(ρz) procedures. In *Microbeam Analysis*; Newbury, D.E., Ed.; San Francisco Press: San Francisco, CA, USA, 1988; pp. 239–246.
58. Claoué-Long, J.C.; Compston, W.; Roberts, J.; Fanning, C.M. Two carboniferous ages: A comparison of SHRIMP zircon dating with conventional zircon ages and $^{40}Ar/^{39}Ar$ analysis. In *Berggren, Geochronology Time Scales and Global Stratigraphic Correlation*; Berggren, W.A., Kent, D.V., Aubrey, M.P., Hardenbol, J., Eds.; Society of Sedimentary Geology Special Publication: Tulsa, OK, USA, 1995; pp. 3–21.
59. Goemann, K.; Donovan, J.J. Electron probe microanalysis of complex natural sulphides using shared background measurements. In Proceedings of the 14th Biennial Australian Microbeam Analysis Symposium (AMAS 2017), Brisbane, Australia, 6–10 February 2017; pp. 61–62, ISBN 978-0-9580408-6-0.
60. Goemann, K.; Donovan, J.J.; Feig, S.T.; Thompson, J. "Sharing" Background Measurements in Wavelength Dispersive Electron Probe Microanalysis. In Proceedings of the Micronalysis Society—Topical Conference on Electron-Probe Microanalysis, Program Guide with Abstracts, Madison, WI, USA, 16–19 May 2016; pp. 28–29, ISBN 978-1-5323-0217-6.
61. Goemann, K.; Donovan, J.J.; Feig, S.T.; Thompson, J. Shared backgrounds in wavelength-dispersive electron probe microanalysis. In Proceedings of the 15th European Workshop on Modern Developments and Applications in Microbeam Analysis, 7th Meeting of the International Union of Microbeam Analysis Societies, Konstanz, Germany, 7–11 May 2017; pp. 378–379, ISBN 978-90-8827-693-0.
62. Donovan, J.J.; Rowe, M. Techniques for Improving Quantitative Analysis of Mineral Glasses. *Geochim. Cosmochim. Acta* **2005**. Goldschmidt abstracts.
63. Donovan, J.J.; Tingle, T.N. An Improved Mean Atomic Number Background Correction for Quantitative Microanalysis. *Microsc. Microanal.* **1996**, *1*, 1–7. [CrossRef]
64. Donovan, J.J.; Singer, J.W.; Armstrong, J.T. A new EPMA method for fast trace element analysis in simple matrices. *Am. Mineral.* **2016**, *101*, 1839–1853. [CrossRef]